This peer-reviewed article has been accepted for publication in Publications of the Astronomical Society of Australia but not yet copyedited or typeset, and so may be subject to change during the production process.

The article is considered published and may be cited using its DOI. 10.1017/pasa.2026.10238

A FLASH H I absorption search in compact sources in the pilot ASKAP interplanetary scintillation field

Paris E. Gordon-Hall [1,2] Emily F. Kerrison [1,2] Elizabeth K. Mahony [2] Elaine M. Sadler [1,2] Hyein Yoon [3,1] J.N.H.S. Aditya [1,4] James R. Allison [5] Rajan Chhetri [6] Ron Ekers [2] Marcin Glowacki [7,8,9] John Morgan [6] Vanessa A. Moss [2] William Roster [10] Mara Salvato [10] Renzhi Su [4] and Matthew Whiting [2]

[1]Sydney Institute for Astronomy, School of Physics A28, The University of Sydney, NSW 2006, Australia
[2]ATNF, CSIRO Space and Astronomy, PO Box 76, Epping, NSW 1710, Australia
[3]Korea Astronomy and Space Science Institute, 776 Daedeok-daero, Yuseong-gu, Daejeon 34055, Korea
[4]Shanghai Astronomical Observatory, Chinese Academy of Sciences, Shanghai 200030, China
[5]First Light Fusion Ltd., Unit 9/10 Oxford Pioneer Park, Mead Road, Yarnton, Kidlington OX5 1QU, UK
[6]ATNF, CSIRO Space and Astronomy, PO Box 1130, Bentley, WA 6102, Australia
[7]Institute for Astronomy, University of Edinburgh, Royal Observatory, Edinburgh EH9 3HJ, UK
[8]Inter-University Institute for Data Intensive Astronomy, Department of Astronomy, University of Cape Town, Cape Town, South Africa
[9]International Centre for Radio Astronomy Research (ICRAR), Curtin University, Bentley, WA, Australia
[10]Max Planck Institute for Extraterrestrial Physics, 85748 Garching near Munich, Germany
Author for correspondence: P.E. Gordon-Hall, Email: pgor0063@uni.sydney.edu.au.

Abstract

In this pilot study, we use data from the First Large Absorption Survey in H I (FLASH) to search for redshifted H I 21 cm absorption at $0.4 < z < 1$ towards 157 bright radio sources with Interplanetary Scintillation (IPS) measurements at 820 MHz in a single field observed with the Australian Square Kilometre Array Pathfinder (ASKAP) radio telescope. The ASKAP IPS measurements, which use only 2.5 minutes of observing time in total, allow us to estimate the compactness of these radio sources on sub-arcsecond scales at a frequency within the 712–1000 MHz FLASH band. In particular, the Normalised Scintillation Index (NSI) for each source reflects the fraction of the flux density arising from compact components less than 0.1 arcsec in diameter. We find that $18 \pm 5\%$ of ASKAP sources with flux densities above 150 mJy are highly compact with NSI ≥ 0.8 – implying that at least 80% of their radio emission arises from a single region smaller than about 800 pc in size. The compactness of these sources makes them ideal probes for an H I absorption search, since the covering factor for any H I gas clouds along the line of sight is likely to be high. About half of the sources with NSI ≥ 0.8 also have peaked radio spectral energy distributions (SEDs), consistent with previous IPS studies at lower frequencies. These pilot results imply that IPS measurements with ASKAP can provide a simple and powerful tool for identifying uniform samples of compact radio sources at frequencies of a few hundred MHz across large areas of sky. With FLASH, we detect two new H I absorption lines against compact sources in the $\sim 30\,\mathrm{deg}^2$ region of sky covered by the IPS data; an associated H I line at redshift $z = 0.9540$ (with a matching optical redshift) in MRC 2125-237 (NSI = 0.98), and a likely intervening line at $z = 0.4632$ towards MRC 2131-241 (NSI = 0.84). The radio sources with these two detections are both bright and compact, with peaked radio SEDs.

Keywords: galaxies: active - galaxies: compact - methods: observational - radio lines: galaxies - radio continuum: galaxies

1. INTRODUCTION

Cold neutral atomic hydrogen (H I) is a tracer for the reservoir of fuel for star formation, and studies of H I are therefore important in understanding the formation and evolution of galaxies. Absorption lines in the spectra of background quasars can be used to study the cosmic evolution of the baryon content of the Universe (Péroux & Howk, 2020), and H I 21 cm absorption lines can also probe the column density of cold H I between the observer and a background source. Unlike emission, the detection limit for an H I 21 cm absorption line is independent of redshift, and is limited only by the spin temperature of the H I gas, the availability of suitably-bright background radio sources that can be used as probes, and the receiver bandwidth (which determines the frequencies that H I 21 cm absorption can be observed).

The First Large Absorption Survey in H I (FLASH) is a wide-field radio survey for H I 21 cm line absorption in the intermediate redshift range $0.4 < z < 1.0$ (look-back times of 4–8 Gyr; Allison et al., 2022; Yoon et al., 2025). FLASH covers 24,000 deg^2 of sky, and is one of nine key Survey Science Projects being carried out with the Australian Square Kilometre Array Pathfinder (ASKAP; Hotan et al., 2021).

H I 21 cm line absorption is classified as either associated or intervening. Associated lines are where the neutral gas causing the absorption is intrinsic to the radio source or quasar. Intervening lines are where the neutral gas is lying along the line of sight to the quasar in a separate galaxy. For associated H I absorption lines the detection rate using FLASH pilot survey data was measured by Su et al. (2022a) and Aditya et al. (2024) and was found to be 2.9% and 1.8% respectively (Yoon et al., 2025). Intervening lines are usually narrower than associated lines as shown by Curran (2021), and they used a literature compilation of known associated and intervening H I absorption lines to show that the median linewidth for intervening absorption

© The Author(s), 2026. Published by Cambridge University Press on behalf of Astronomical Society of Australia. This is an Open Access article, distributed under the terms of the Creative Commons Attribution licence (https://creativecommons.org/licenses/by/4.0/), which permits unrestricted re-use, distribution and reproduction, provided the original article is properly cited.
https://doi.org/10.1017/pasa.2026.10238 Published online by Cambridge University Press

lines was significantly lower than the median linewidth for associated lines. In FLASH data, narrower lines are harder to detect and are possibly misidentified as spectral artefacts (Yoon et al., 2025, Section 9.3).

Several targeted searches in H I found that radio continuum sources with H I absorption were usually compact, including both compact steep-spectrum (CSS) and peaked-spectrum (PS) sources (e.g. Véron-Cetty et al., 2000; Vermeulen et al., 2003; Pihlström et al., 2003; Gupta et al., 2006; Chandola et al., 2011; Geréb et al., 2015; Maccagni et al., 2017; Morganti & Oosterloo, 2018; Aditya et al., 2024; Yoon et al., 2025).

CSS and PS sources are compact and strong radio sources which are believed to be young radio AGN (O'Dea, 1998; O'Dea & Saikia, 2021). The radio spectra of the intrinsically small PS sources can appear peaked due to either synchrotron self-absorption or free-free absorption (O'Dea & Saikia, 2021). The frequency of the peak in a synchrotron self-absorbed source scales inversely with the angular size of the source, so more compact radio sources are expected to peak at higher frequencies (O'Dea & Saikia, 2021). Some earlier publications have discussed separate classes of GHz-Peaked-Spectrum (GPS) sources, High Frequency Peakers (HFPs), and Megahertz Peaked-Spectrum (MPS) sources. In this work, we refer to all these objects as PS sources.

Large and unbiased catalogues of PS radio sources are now becoming available through the combination of large-area radio continuum surveys across a wide frequency range (e.g. Callingham et al., 2017; Slob et al., 2022; Kerrison et al., 2025).

Interplanetary scintillation (IPS) can produce rapid fluctuations in the intensity of radio waves as they travel through density variations in the solar wind (Clarke, 1964; Hewish et al., 1964). These fluctuations reduce rapidly for sources larger than some characteristic diameter (~ 0.1 arcseconds at 800 MHz), so measurements of IPS allow us to identify sub-arcsecond scale compact components in low-frequency radio sources.

Morgan et al. (2018) showed that the Murchison Widefield Array (MWA; Tingay et al., 2013) could be used to carry out wide-field IPS measurements across large areas of sky at 160 MHz. This makes it possible to assemble large samples of compact low-frequency radio sources without the complexity associated with low-frequency long-baseline interferometry.

Chhetri et al. (2018) presented the first astrophysical application of the technique of wide-field IPS with the MWA. They used five minutes of data observed at 162 MHz with 0.5 s time resolution to detect 2550 bright continuum sources across a single 900 deg^2 field. They also introduced the concept of a *normalised scintillation index* (NSI) to remove the effects of solar elongation on the observed level of scintillation.

They found that around 12 % of sources in this field demonstrated rapid fluctuations caused by IPS, indicating compact structures. They find 9 % of bright sources have an NSI ≥ 0.9 which they define as strongly scintillating, implying that ≥ 90 % of their low-frequency emission arises from a sub-arcsecond compact component.

Interestingly, they also found that PS radio sources were the dominant population within strongly scintillating, low-frequency sources in their sample. In a follow-up paper, Sadler et al. (2019) showed that the strongly scintillating MWA sources were a relatively distant population, with a median redshift of $z \sim 1.5$, and that at least 30 % of them were likely to lie at $z > 2$. Compact (scintillating) sources at these redshifts are ideal targets for H I absorption studies.

Aditya et al. (2024) found that two out of the three objects with detected H I absorption in their sample show IPS at 162 MHz. Both of these objects were also compact with high NSIs. They suggest IPS as an efficient alternative to VLBI in finding compact sources which have an expected higher H I detection rate (e.g. Curran et al., 2013).

Chhetri et al. (2023) used measurements of a single bright source to show that the wide-field IPS technique could be extended to higher frequencies using ASKAP at 862 MHz with the CRAFT coherent (CRACO) fast transient system (Wang et al., 2025). Following this, Chhetri et al. (2026) used all 36 phased array feed (PAF) beams of ASKAP to make the first wide-field IPS observations with ASKAP.

In this paper, we combine the Chhetri et al. (2026) IPS catalogue for a single ASKAP field with FLASH (Allison et al., 2022) spectral-line observations of the same field, to search for H I absorption against the ASKAP IPS sources. In Section 2, we discuss how the ASKAP IPS compact source sample was selected, and how it was crossmatched with FLASH to produce the final catalogue of sources focused on in this work. In Section 3, we explain the use of `RadioSED` to fit the radio spectral energy distributions with models that show if the source is likely PS or not. In Section 4, we show the Legacy Survey (Dey et al., 2019a) images for the key sources of this paper, and any optical redshifts and counterparts. In Section 5, we explain the process of searching for H I absorption lines, and show the two detections found from the sample of sources searched. In Section 6, we discuss the properties of the two H I detections. In Section 7, we discuss the nature of the sources with H I detections, and the H I detection rate. We also discuss the NSI and spectral index relationship, and in particular a source with unusual measurements, the connection between NSI and optical classification, as well as possible future work. In Section 8, we summarise the key findings in this paper. Throughout this paper, we assume a flat, Λ, cold dark matter (ΛCDM) cosmology with values from Planck Collaboration et al. (2020); $H_0 = 67.4\,\mathrm{km\,s^{-1}\,Mpc^{-1}}$, $\Omega_M = 0.315$, and $\Omega_\Lambda = 1 - 0.315$.

2. THE ASKAP IPS COMPACT SOURCE SAMPLE

2.1 ASKAP IPS data

We use the ASKAP IPS data from Chhetri et al. (2026) to estimate the compactness of the radio sources that have been searched for H I absorption by FLASH. The ASKAP IPS observations used the CRACO system to measure flux densities at 110 ms intervals. These observations were made on 2023 February 2, with 16 observations around the Sun covering solar elongations between 7.5 and 12.5 degrees. The IPS observations were carried out as part of technical tests to determine the feasibility for expanding on IPS work in future, making use

https://doi.org/10.1017/pasa.2026.10238 Published online by Cambridge University Press

of the autonomous scheduling and science operations system implemented for ASKAP (Moss et al. (in prep.)).

The ASKAP IPS data pipeline produces images made at 110 ms intervals ("snapshot images"), as well as single images for the full duration of the observation (called a "standard image"), for each ASKAP beam separately. The "variability image" for each beam is then produced by first applying a filter to remove time variations from the ionosphere to emphasise timescales associated with IPS. Then the standard deviation for each pixel in the snapshot images is taken along the time axis (described further in Morgan et al., 2018; Chhetri et al., 2018). Sources with variance due to IPS have high standard deviation, meaning that only sub-arcsecond scale compact sources remain in the variability image. This makes the identification of compact sources much easier.

The Aegean source finder (Hancock et al., 2018) was used to identify the scintillating compact sources in the variability image. For each source, a scintillation index was derived by comparing the scintillation flux density from the variability image with the mean flux density from the standard image. A normalised scintillation index (NSI) was then calculated by dividing the observed scintillation index by the predicted scintillation index (calculated using a simple empirical relationship (Hewish & Symonds, 1969; Rickett, 1973; Chhetri et al., 2018)), making it possible to compare the scintillation properties of all the sources in the field by removing the effect of solar elongation (Chhetri et al., 2018). Chhetri et al. (2026) also estimated upper limits on the NSI for sources that were detected in the standard image, but not in the variability image. We note that some sources have NSIs above 1, and high NSI uncertainty which is potentially due to measurement issues. Finally, these authors measured a 'compact' flux density for each source - representing the flux density contained within a region ~ 0.1 arcsec in size. This was derived by multiplying the peak flux density of each source by its measured NSI value.

2.2 FLASH data in the ASKAP IPS field

Two FLASH survey fields, listed in Table 1, overlap the single ASKAP IPS field analysed by Chhetri et al. (2026). Figure 1 shows the radio continuum sources in the two FLASH fields as well as the positions of all the ASKAP IPS sources (including those not covered by FLASH) shown in the Appendix in Tables 9 and Table 10.

Processed FLASH data products for both fields are available from the public CSIRO ASKAP Science Data Archive (CASDA), and include continuum source catalogues (at a central frequency of 856 MHz and with 12-15 arcsec resolution) produced by the Selavy source finder for each field (Whiting & Humphreys, 2012).

The quality of each processed FLASH observation was checked by members of the science team, who provided validation notes to accompany the CASDA data release. As discussed by Yoon et al. (2025), the FLASH data are largely free from terrestrial radio frequency interference (RFI), though small regions of data can be affected by spectral-line artefacts which was a factor in these datasets.

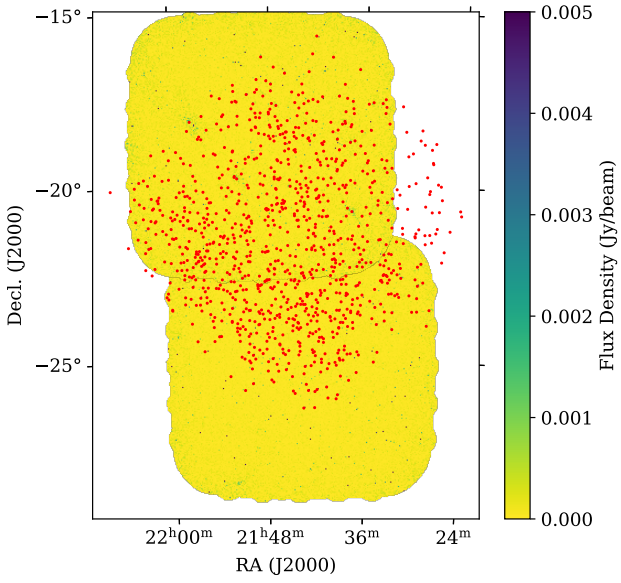


Figure 1. The radio continuum images of the two FLASH fields, SBID55464 and SBID62794, with the ASKAP IPS source locations overlaid on top shown by the red points. There is some overlap between the two FLASH fields.

The continuum island source catalogues (see Yoon et al. (2025) for further description) for FLASH fields 350 (SBID 55464) and 405 (SBID 62794) were each crossmatched separately with a combined ASKAP-MWA IPS catalogue (prepared by Chhetri et al. (2026)) as outlined in Table 2. We selected a large search radius of 30 arcseconds to encompass all possible matches, and then only included the best match for each ASKAP IPS source. Since these FLASH fields overlap, some sources had a match in both FLASH fields. Both of these matches were included in the final catalogue. The number of IPS continuum sources is smaller than the number of FLASH continuum detections because of the very short IPS observing time (2.5 minutes (Chhetri et al., 2026)); compared to the much deeper FLASH catalogue with an integration time of two hours per field (Allison et al., 2022; Yoon et al., 2025). There are also significantly fewer sources once only scintillating sources are selected in the variability image. From the crossmatched catalogue, we selected only sources with a FLASH integrated flux density $S_{856\mathrm{MHz}} \geq 30$ mJy, which is the limit for spectrum extraction for most FLASH fields. This limit is imposed to balance processing time, data volume, and overall efficiency since the detection of H I in the FLASH spectral-line data is not likely for fainter sources (Yoon et al., 2025). Chhetri et al. (2026) found that the ASKAP IPS observations are complete for compact components above 150 mJy/beam down to NSI 0.1 - i.e. they detect all compact components with flux density $S_{820\mathrm{MHz}} > 150$ mJy. Sources with high NSI values can be detected down to total flux densities well below 150 mJy.

Finally, we selected two separate FLASH-IPS samples:

(a) **The bright-source sample**. This sample contains the 88 sources that lie within the FLASH footprint and have both

https://doi.org/10.1017/pasa.2026.10238 Published online by Cambridge University Press

Table 1. Pointing centres, integration times, observation dates, sky coverage and central frequencies of the two ASKAP FLASH fields used in this study. The SBID is the observation number listed in the CASDA archive.

Field	SBID	RA_J2000 (hms)	Dec_J2000 (dms)	Integration time (hrs)	Date observed	Sky coverage (deg^2)	Central frequency (MHz)
FLASH 350	55464	21:44:09.20	-25:07:52.0	2	17-12-2023	6.4 x 6.4	855.5
FLASH 405	62794	21:49:05.59	-18:51:49.0	2	11-06-2024	6.4 x 6.4	855.5

peak flux density $\geq$ 150 mJy and continuum S/N $\geq$ 20 in the ASKAP IPS catalogue. The S/N limit ensures that all the included sources are in regions of the ASKAP IPS field where the upper limits on NSI are restrictive, so that this sample can be used for statistical analyses. The bright-source sample contains 59 objects with detected NSI, and 29 with upper limits in NSI.

(b) **The additional sample**. This sample contains a further 69 sources that lie within the FLASH area and have flux density $\geq$ 30 mJy, but do not meet the criteria for inclusion in the bright-source sample. Only sources with detected scintillation, and a measured NSI value are included in the additional sample, since the upper limits on NSI are not generally restrictive in this flux density range.

Table 2. A summary of the number of sources in each crossmatching step, after filtering for bright sources with an ASKAP NSI, and in the final two samples of sources searched for H I absorption.

Sample	Number
ASKAP-MWA IPS catalogue	1026
FLASH Field 350 (SBID 55464)	15901
FLASH Field 405 (SBID 62794)	11192
Crossmatch of FLASH and IPS (includes duplicate matches)	1137
Unique sources $\geq$30 mJy with NSI detection (after removing duplicates)	128
Bright-source sample ($\geq$ 150 mJy, includes NSI upper limits)	88
Additional sample (other FLASH sources, NSI det. only)	69

3. RADIO SED FITTING

3.1 Fitting method

To determine which of our sources had a peaked radio spectrum, we fitted the radio Spectral Energy Distributions (SEDs) for each of the 157 sources in the bright-source and additional samples.

The SED fitting was done using radio flux density measurements from the 888 MHz Rapid ASKAP Continuum Survey (RACS) (McConnell et al., 2020) as well as several other large-area, publicly available continuum surveys. These included the Galactic and Extragalactic All-Sky MWA Extended Survey (GLEAM-X) (76-227 MHz) (Hurley-Walker et al., 2022), the NRAO VLA Sky Survey (NVSS) (1.4 GHz) (Condon et al., 1998), the Very Large Array Sky Survey (VLASS) (3 GHz) (Lacy et al., 2020), the Australia Telescope 20 GHz Survey (AT20G) (5, 8, 20 GHz) (Murphy et al., 2010).

Modelling of the SEDs was done with `RadioSED`, a package designed to be used with broadband radio continuum data (Kerrison et al., 2024). This code performs Bayesian inference using nested sampling (Skilling, 2004). Four models are implemented including a simple power law, a log-space parabola (described in Dallacasa et al. (2000) and Orienti et al. (2007)), a functional form for a PS source, which reduces to a synchrotron self-absorbed source under the condition k=2.5 (Snellen et al., 1998), and a 'retriggered' model comprising the functional form from Snellen et al. (1998) combined with an additional power law component. `RadioSED` infers which of these analytical models is the best fit for each SED.

Tables 9 and 10 list the full data table, displaying the source name, alternate NED name, object type, coordinates, photometric redshift, spectroscopic redshift, ASKAP NSI, and SED result.

3.2 SED properties of the bright-source sample

Table 3 shows the distribution of SED fits for the 88 sources in the bright-source sample with S $\geq$ 150 mJy, which represents the general galaxy population at this flux density level. Since we include sources that only have an NSI upper limit in the bright-source sample, which are assumed to be extended sources, and peaked sources are only compact sources, we find as expected that most of the sources in this sample are best-fitted by power law radio spectra.

Table 3. Radio SED distribution for the 88 sources in the bright-source (S $\geq$ 150 mJy) sample.

SED class	Number	Fraction
Power law	72	82%
Peaked	12	14%
Flat/inverted	4	4%
Total	88	

Peaked radio SEDs are found in 14% of sources in Table 3. This is roughly consistent with the $\sim$ 10% fraction found in bright-source samples at GHz frequencies (O'Dea, 1998) and the value of 9% for PS sources in the MWA IPS sample (Chhetri et al., 2018; Sadler et al., 2019). We see no evidence for a variation in the PS fraction with flux density in the current (relatively small) sample of 88 sources.

Before moving to a more general discussion of the relationship between source size and radio SED, we first summarise the distribution of NSI values within this flux density-limited sample. The relationship is discussed in detail for a larger ASKAP IPS sample by Chhetri et al. (2026), but Table 4 shows the breakdown for the two IPS samples used in the current paper to search for H I absorption lines.

https://doi.org/10.1017/pasa.2026.10238 Published online by Cambridge University Press

Table 4. ASKAP NSI distributions for the 88 sources in the bright-source sample and the 69 sources in the additional sample.

Source type	NSI	Bright-source sample	Additional sample
Compact	≥ 0.8	16 (18%)	45 (65%)
Partly resolved	0.4–0.8	16 (18%)	20 (29%)
Extended	≤ 0.4	48 (55%)	4 (6%)
Unclear (NSI upper limit > 0.4)		8 (9%)	
Total		88	69
Median NSI		0.26 ± 0.05	

The median ASKAP NSI value for the bright-source sample is 0.26 ± 0.05, which we can consider to be representative of the overall source population at this flux density level. For the fainter additional sample, the median NSI is 0.88 ± 0.16. We know that this will be biased towards sources with high NSI values (compact sources) since NSI upper limits are not included in the additional sample. For this reason, the additional sample's median NSI is not included in Table 4.

3.3 SED properties of compact and resolved sources

Table 5 shows the distribution of radio SED classes, fitted as either peaked, power law, or flat (which included sources with an inverted radio spectrum), for the bright-source sample and additional sample, split by NSI value into compact (NSI ≥ 0.8), slightly resolved ($0.4 <$ NSI < 0.8), or extended (NSI ≤ 0.4) sources. As explained in Section 1, the NSI represents the fraction of the low-frequency emission from the source arising from a sub-arcsecond compact component. We include the additional sample here as well as the bright-source sample so that our statistics were not biased towards bright sources.

As seen in Table 5, almost half of the compact sources have peaked radio spectra, as was also found by Chhetri et al. (2018) at the lower MWA frequency of 162 MHz, while all of the extended sources are fitted by a power law. Only 9% of the compact sources have flat or inverted radio spectra. Note that IPS cannot yet be used to differentiate between a slightly resolved compact structure or a point source embedded in a completely resolved extended structure. A source with a slightly resolved NSI could be a double with unresolved components, or a single compact source with some extended emission resolved out (see Morgan et al., 2019, Figure 5 for source morphologies consistent with a particular NSI).

4. OPTICAL IDENTIFICATIONS AND REDSHIFTS

4.1 Optical counterparts of the FLASH-IPS sources

We used the FLASH optical ID catalogue made by Roster et al. (2026) to identify optical counterparts for the FLASH-IPS sources listed in Tables 9 and 10. These authors used machine learning techniques to identify the counterparts of $\sim 80,000$ unresolved (angular size $< 10 - 15$ arcsec) radio sources from the FLASH survey by crossmatching the radio positions with optical images from the DESI Legacy Imaging Surveys Data Release 10 (LS10; Dey et al., 2019b). LS10 provides four-band

Table 5. Radio SED distribution for compact, resolved, and extended sources with NSI detections or upper limits. This table includes all 157 sources from the bright-source sample and additional sample.

		Radio SED fit			
Source type	NSI	Peaked	Power law	Flat/Inv	Total
Compact	≥ 0.8	27	26	5	58
		(47%)	(45%)	(9%)	(37%)
Partly	0.4–0.8	5	31	3	39
resolved		(13%)	(79%)	(8%)	(25%)
Extended	≤ 0.4	0	60	0	60
		(0%)	(100%)	(0%)	(38%)

griz images and catalogues for much of the southern sky, as well as classification of each catalogued object as either an optical point source (PSF) or one of four classes of galaxies: round exponential galaxies with a variable radius ("REX"), de-Vaucouleurs ("DEV") profiles (elliptical galaxies), exponential ("EXP") profiles (spiral galaxies), and Sersic ("SER") profiles. The catalogue made by Roster et al. (2026) also includes photometric redshift estimates derived using the PICZL code (Roster et al., 2024). The optical identifications and photometric redshifts from the Roster et al. (2026) catalogue were accepted if the optical counterpart probability $p_{\rm any}$ had a value above 0.29. This cutoff provides a good compromise with roughly 80% purity and 80% completeness, corresponding to an estimated chance-association rate of $\sim 20\%$ (Roster et al., 2026).

Unfortunately, the LS10 imaging in the ASKAP IPS field is incomplete, with images for much of the region only available in one or two of the four bands. For this reason, we grouped the four optical galaxy classes together, and classified each object as either a quasar (LS10 PSF classification), or a galaxy. The photometric redshifts listed in Tables 9 and 10 should also be regarded as indicative in many cases, especially for those with $z > 2$.

We also searched the NASA/IPAC Extragalactic Database (NED) for optical spectroscopic redshifts of sources in the FLASH-IPS sample. This yielded 16 redshift measurements (9 galaxies and 7 quasars). Redshifts for a further 11 quasars are available from Gaia spectra as listed in the Quaia catalogue (Storey-Fisher et al., 2024).

Optical counterparts and photometric redshift estimates are available for 54 of the 88 sources in the bright-source sample (Table 9), and 48 of the 69 sources in the additional sample (Table 10).

We can be confident that all the radio sources in Tables 9 and 10 are genuine; they are many times brighter than the ~ 0.5 mJy detection limit of the FLASH images and also appear in catalogues from the earlier NVSS (Condon et al., 1998) and RACS (Hale et al., 2021) radio surveys. However, about 30% of radio sources in Tables 9 and 10 do not have a listed optical counterpart, and there are several reasons for this:

- *Extended radio sources:* Around 10% of FLASH sources are extended on scales larger than 15–30 arcsec, and resolved into two or more components in ASKAP images. Since identifying optical counterparts for these sources is more

https://doi.org/10.1017/pasa.2026.10238 Published online by Cambridge University Press

challenging (see e.g. Best et al., 2005; Ching et al., 2017), they were not included in the Roster et al. (2026) catalogue.
- *Ambiguous optical counterpart:* In a few cases, two similar objects are visible on the LS10 images, and the PICZL code is unable to determine which is the more likely counterpart. It is also possible that both objects could contribute to the observed radio emission.
- *Low-probability optical counterpart:* Here, a potential counterpart is visible on the LS10 images, but is unlikely to be associated with the radio source. The true counterpart may be a more distant galaxy that is not visible, or the radio-optical offset may be large enough that we cannot be confident that the association is genuine.
- *Blank field:* The counterpart is fainter than the detection limit of the LS10 optical images, typically > 21.5 mag in g and r in the ASKAP IPS region (Saxena et al., 2024).
- *Foreground stars:* In a small number of cases (e.g. J214032.5-211559 and J214011.6-182529 in Tables 9 and 10), the presence of a bright Galactic foreground star means that reliable photometry is not available for nearby objects.

4.2 Redshift distribution

Figure 2 shows a stacked histogram of the photometric redshifts and spectroscopic redshifts separately and split into either quasars or galaxies, as was also done by Kerrison et al. (2025). A small number of galaxies with PICZL photometric redshifts of $z > 2$ are not included in this diagram. Unlike quasars, most galaxies with $z > 1.5$ are too faint to be visible in the LS10 images (Roster et al., 2026). The high photometric redshifts estimated for these few objects are likely to be unreliable due to the low SNR and missing bands in the LS10 photometry.

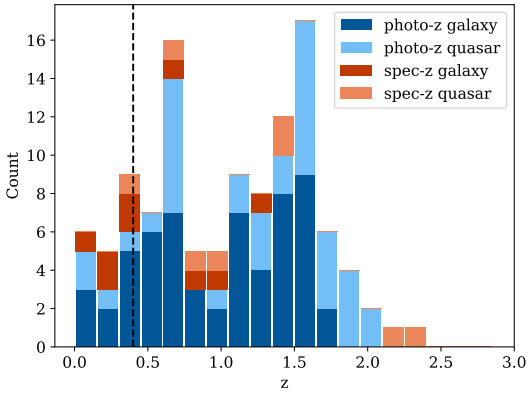


Figure 2. Histogram of the photometric and spectroscopic redshifts for sources divided into whether they were classified as either quasars or galaxies. Photometric is shown in blue, and spectroscopic is shown in striped orange with the paler colours showing quasars and darker colours showing galaxies. The two photometric redshift outliers are not shown in the diagram. The dashed vertical line is at $z = 0.4$.

5. H I ABSORPTION-LINE SEARCH

We use the FLASH spectral-line data to search for H I 21 cm absorption against the sources listed in Tables 9 and 10. This is an untargeted search in the sense that we search across the full FLASH redshift range ($0.4 < z < 1.0$) for all objects, and do not apply any form of optical preselection.

5.1 H I absorption search

Spectral-line profiles and linefinder results were collected from the FLASH database after validation by the FLASH team. FLASHfinder is a Bayesian line-finding tool (Allison et al., 2012) designed to make an automated search for H I absorption lines in large ASKAP spectral-line datasets (e.g. Glowacki et al., 2019; Allison et al., 2020; Sadler et al., 2020; Allison et al., 2021; Mahony et al., 2022; Su et al., 2022b; Aditya et al., 2024; Yoon et al., 2025). FLASHfinder is run on the extracted spectra from each SBID, and a single Gaussian component is fit to each candidate line. The output data file includes measurements and uncertainties of: the redshift of the peak of the candidate line, the peak optical depth of the line, the integrated optical depth of the line, the FWHM linewidth with a single Gaussian fit of the line, and the Bayesian evidence value ln (B). The ln (B) parameter quantifies how likely it is that the line detection exists compared to the null hypothesis, which is where no line is present. The median rms noise level of the spectra is around 5.5 mJy beam^{-1} (Yoon et al., 2025).

The output file contains all candidate detections which could be astronomical signals or artefacts, and only candidates with a ln (B) value above 30 were considered as robust detections in this paper. As explained by Yoon et al. (2025), a conservative approach is to consider lines for which ln (B) ≥ 30 because when the original spectra are inverted and the linefinder is re-run, only spectral artefacts and noise should be seen. As shown in their Figure 11, ln (B) ~ 30 is an upper envelope to most of the linefinder points from the inverted spectrum. However, they acknowledge that choosing this value of ln (B) has likely resulted in some true absorption lines being missed. Since the ASKAP IPS catalogue only covers two FLASH SBIDs, ln (B) values down to 10 were checked by visual inspection to identify potential detections. An expectation is that only one or two spectra will contain H I absorption in an SBID, while spectral artefacts will typically occur in the same frequency position in multiple spectra.

5.2 H I detections

Two strong H I absorption lines were detected, in J212805.5-232946 (with ln B = 127) and J213437.6-235537 (with ln B = 198).

The H I spectra of these two detections are shown in Figures 3 and 4. The parameters fitted by the FLASHfinder are listed in Table 6. Both of the sources with H I detections were identified as PS radio sources by Callingham et al. (2017).

We also investigated 10 tentative detections of weaker lines with ln B values as low as 10. Only one of these was from SBID 55464 (Field 350), while the other nine were from SBID 62794 (Field 405), which is known to have some regions of poorer-quality data. None of these tentative lines were accepted as a robust detection of an H I line. Four of them lay in a narrow spectral region between 832 and 835 MHz (H I z = 0.701 to

https://doi.org/10.1017/pasa.2026.10238 Published online by Cambridge University Press

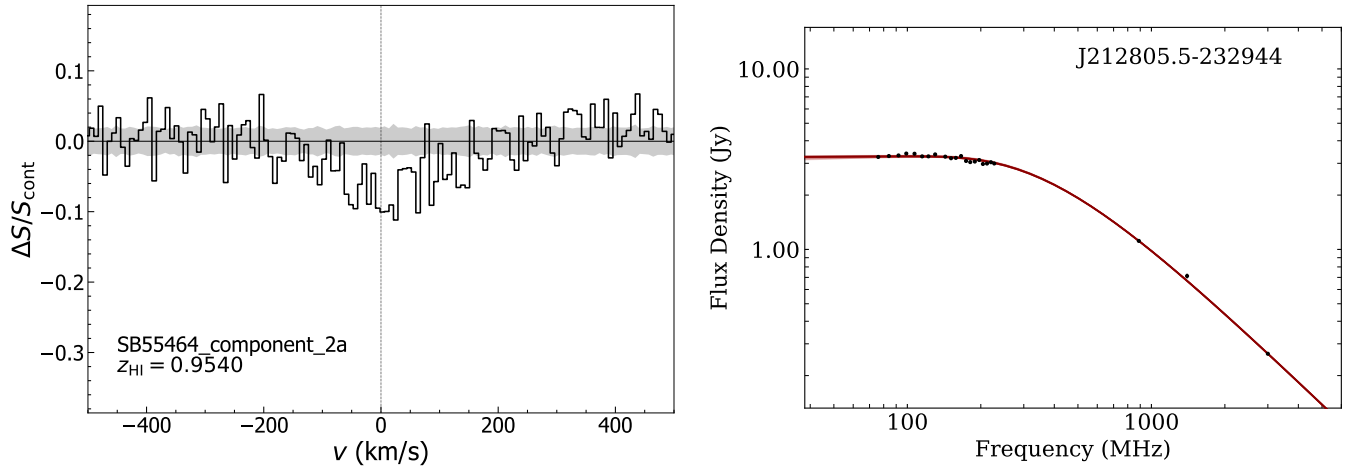


Figure 3. The H I absorption spectral-line profile on the left, and radio SED fit for J212805.5-232944 (MRC 2125-237) on the right. The velocities are relative to $z = 0.9540$. The grey band in the spectra shows the rms spectral-line noise (Yoon et al., 2025). The favoured model is peaked, with a Bayes factor of of 4.4.

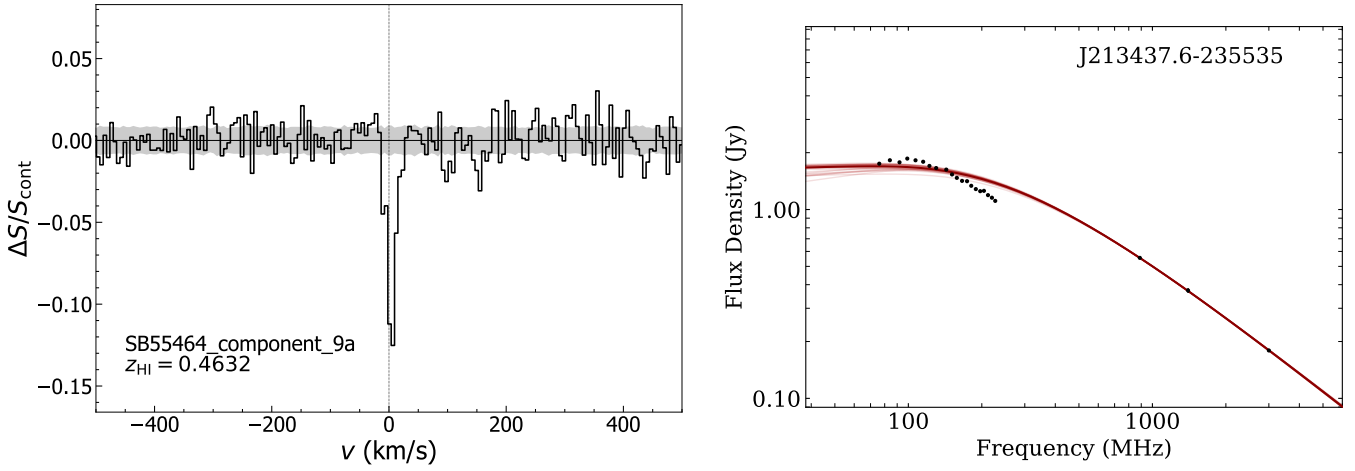


Figure 4. The H I absorption spectral-line profile on the left, and radio SED fit for J213437.6-235535 (MRC 2131-241) on the right. The velocities are relative to $z = 0.4632$. The grey band in the spectra shows the rms spectral-line noise (Yoon et al., 2025). The favoured model is peaked, with a Bayes factor of 1.8. This source demonstrates that the model does not always provide a perfect fit, reflecting the increased complexity or variability in some cases.

0.707) where the spectral-line noise in SBID 62794 is higher than usual, which is likely due to the tropospheric ducting of RFI, (see Yoon et al. (2025) for a description of how ducting affects the spectra). Two are at the position of known correlator artefacts, and the remaining four have ln B < 20, and are statistically likely to be noise peaks.

5.3 Upper limits for non-detections

For sources with no H I detection, the upper limit of the peak optical depth was calculated using the equation for peak optical depth τ given by:

$$I/I_0 = e^{-\tau}$$

where I_0 is the peak flux density of the source, I is the observed flux density at the peak of the line, and $(I_0 - I)$ is the size of the 'dip' below the continuum level. For an upper limit, where σ is the rms noise in a single spectra channel, and we assume a detection limit of 5σ, the equation becomes:

$$\tau = -\ln[(I_0 - 5\sigma)/I_0]$$

We assume a value of $\sigma \sim 5.5$ mJy.beam^{-1} per spectral channel. Tables 9 and 10 show the upper limits of the peak optical depth for the sources with no H I detections, and we present the upper limits of the peak optical depth for all the sources with non-detections, sources with tentative detections, as well as the peak optical depth for the two H I detections against the integrated flux density in Figure 5.

6. PROPERTIES OF THE H I DETECTIONS

The LS10 images at the positions of the two sources (shown in Table 7) with detections of H I absorption are shown in

https://doi.org/10.1017/pasa.2026.10238 Published online by Cambridge University Press

Table 6. The two H I absorption detections with FLASHfinder results for the spectra; (1) Source name; (2) FLASH field name; (3) H I redshift; (4) Peak optical depth upper limit (except for detections) and uncertainty; (5) Integrated optical depth and uncertainty; (6) Linewidth and uncertainty; (7) ln (B); (8) FLASH integrated flux density (mJy) at 855.5 MHz. The uncertainties in columns (4) to (6) represent the 68% interval around the median. The table is based on Tables 5 and 6 in Yoon et al. (2025).

Source name	FLASH field	$z_{\rm H\,I}$	$\tau_{\rm peak}$	$\tau_{\rm int}$ (km s^{-1})	Width (km s^{-1})	ln (B)	FLASH integrated flux density (mJy)
(1)	(2)	(3)	(4)	(5)	(6)	(7)	(8)
MRC 2125-237	350	0.9540	0.075 ± 0.006	$16.08^{+1.15}_{-1.13}$	$215.8^{+18.5}_{-16.9}$	125.7	1145.64
MRC 2131-241	350	0.4632	0.123 ± 0.009	$2.25^{+0.13}_{-0.14}$	$18.2^{+1.4}_{-1.4}$	198.0	535.85

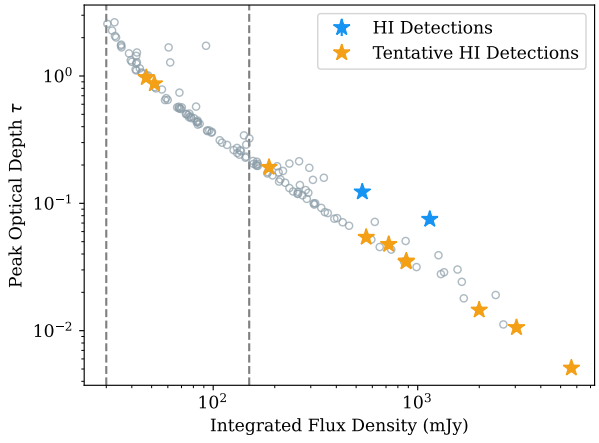


Figure 5. The upper limits of the peak optical depth for non-detections (shown by the grey circles) and the peak optical depths of the H I lines detected (shown by the blue stars) against the integrated flux density. Sources with tentative detections have their upper limits shown by the orange stars. The vertical dashed lines show the 30 mJy limit used for the H I line search, as well as the 150 mJy limit for the bright-source sample.

Figure 6. Both of these objects, MRC 2125-237 (J212805.5-232944) and MRC 2131-241 (J213437.6-235535) are bright radio sources included in the MRC-1Jy catalogue (McCarthy et al., 1996). In each figure, the red circles are centred on the MRC-1Jy radio position with a radius of 5 arcsec on the sky.

The MRC-1Jy catalogue contains sources with a flux density above 1 Jy at 408 MHz, that lie within a strip of the southern sky at declinations between about −20 and −30 degrees. The additional data available for the MRC-1Jy sample includes high-resolution radio images, deep optical images, and (for about half the sample) optical spectra and redshift measurements.

Table 7 lists the radio positions measured for these two sources by Kapahi et al. (1998) using high-resolution continuum images from the VLA at 5 GHz. These positions are expected to be accurate to better than 0.1 arcsec, while the LS10 optical positions are tied to the Gaia reference frame and should generally be accurate to within 0.2 arcsec. The MRC-1Jy radio positions are more accurate compared to the ASKAP positions listed in the main tables (Tables 9 and 10) which have a typical uncertainty of $\sim$ 1 arcsec. Since MRC-1Jy positions are not available for all sources, the ASKAP positions were used for the optical crossmatching in Section 4.

6.1 MRC 2125-237 (J212805.5-232944)

The optical counterpart of the radio source MRC 2125-237 (shown in Figure 6 on the top), is a galaxy whose optical redshift of z = 0.95 ± 0.05 (McCarthy et al., 1996), matches the H I absorption redshift of z = 0.9540 ± 0.0001. This galaxy has an optical $g - i$ colour of 1.69 mag, placing it in the region occupied by high-excitation radio galaxies (HERGs; Heckman & Best, 2014) in this redshift range (Ching et al., 2017). The galaxy has a fainter potential companion 2.5 arcsec away, corresponding to a projected separation of 20 kpc on the sky at the H I redshift.

The broad H I absorption FWHM linewidth of 216 km s^{-1} suggests that this is an associated H I system where the H I gas lies in or around the same galaxy that hosts the radio source (e.g. Curran, 2021). This is also supported by the close match between the optical and H I redshifts. As shown in Curran (2021), the probability of the H I absorber being intervening depends upon the full width at zero intensity (FWZI) of the profile. They find that for values of FWZI below approximately 120 km s^{-1}, there is a high probability (>70%) that the absorber is intervening. For values greater than 120, the probability sharply drops, and for FWZI $\gtrsim$ 200 km s^{-1}, the probability of the absorber being intervening is around 20%. The FWZI for both detections was found by eye from the spectral-line profiles, since these values are not provided in the FLASH linefinder data. For MRC 2125-237 we find the FWZI to be approximately 400 km s^{-1}.

The ASKAP NSI value of 0.98 ± 0.06 implies that almost all the radio emission arises from a region smaller than 800 pc in size, i.e. well within the size range expected for PS radio sources (O'Dea & Saikia, 2021).

6.2 MRC 2131-241 (J213437.6-235535)

McCarthy et al. (1996) provided a finding chart for MRC 2131-241, and identified the optical counterpart as the faint object near the centre of the circle in the lower image in Figure 6, noting that "The identification is a galaxy 1 arcsec northwest of a star." Only g and i band LS10 images are available for this region of sky. Confusingly, the faint object near the centre of the circle, which McCarthy et al. (1996) listed as a galaxy, is classified as a point source (PSF) in the LS10 catalogue; but the brighter object to the south-east, which McCarthy et al.

https://doi.org/10.1017/pasa.2026.10238 Published online by Cambridge University Press

Table 7. Radio and optical positions for the two radio sources with detected H I absorption, and their potential optical counterparts.

Source	MRC-1Jy radio position		MRC-1Jy optical position (J2000)		LS10 optical position		Radio-optical offset (MRC-1Jy-LS10, arcsec)
MRC 2125-237	322.023127	-23.496003	322.023334	-23.495697	322.023141	-23.495966	0.14
MRC 2131-241 (LS10 PSF)	323.657001	-23.926776	..	..	323.656892	-23.926791	0.36
MRC 2131-241 (LS10 galaxy)	323.657001	-23.926776	323.657959	-23.927246	323.657357	-23.927154	1.80

(1996) referred to as a star, is classified by LS10 as a galaxy. Additional high resolution optical imaging would be useful to clarify the nature of these two objects, but we can still draw some conclusions from the data available now.

The narrow H I FWHM linewidth of 18.2 km s^{-1} and FWZI of ∼50 km s^{-1} suggests that this is an intervening line. The faint object closest to the MRC-1Jy radio position also has an *i*-band magnitude of 22.4, which is far fainter than expected for a radio galaxy at the H I redshift of z = 0.4632, again implying that the radio-source host is much more distant than the H I gas seen in absorption. The brighter galaxy offset from the radio position in Figure 6 has a photometric redshift estimate of $z \sim 0.66$, and a $g - i$ colour of 1.85 mag, consistent with the general population of star-forming galaxies at this redshift (Ching et al., 2017). It therefore seems likely that this is an intervening line, with a potential H I host galaxy at an impact parameter of around 10 kpc from the background radio source.

The ASKAP NSI value of 0.84 ± 0.04, as with the previous source MRC 2125-237, implies that most of the radio emission arises from a compact region smaller than ∼ 800 pc in diameter.

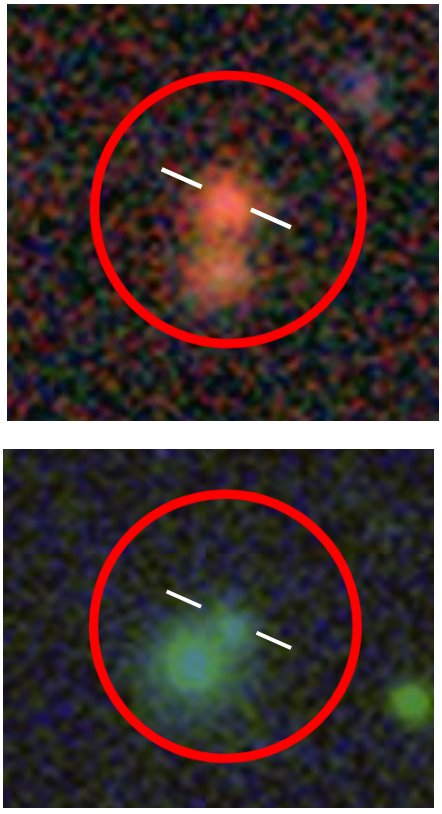


Figure 6. Legacy Survey DR 10 images centred on the MRC-1Jy radio position of MRC 2125-237 (J212805.5-232946) (on the top) and MRC 2131-241 (J213437.6-235537) (on the bottom). The red circle on the two sources has a radius of 5 arcsec, which corresponds to a projected distance of 40.1 kpc on the sky at the H I redshift of z = 0.9540, and 29.6 kpc on the sky at the H I redshift of z = 0.4632 respectively. The two white lines indicate the galaxy identified as the radio-source host.

7. DISCUSSION

7.1 H I detection rate

The H I lines detected in this work from sources MRC 2131-241 and MRC 2125-237 have redshifts of 0.4632 and 0.9540, and FWHM velocity linewidths of 18 km s^{-1} and 216 km s^{-1} respectively. As discussed in Yoon et al. (2025), data validation is completed with a checklist, which then supplies a numerical score which the FLASH team uses to classify each SBID as either GOOD, UNCERTAIN, or BAD. This checklist includes, but is not limited to, measurements of the rms noise, visual inspection of the images, and a sample of spectra. Both of the detections in this work were from the FLASH field 350 (SBID 55464) which had GOOD quality spectral-line data. The other FLASH field 405 (SBID 62794) was validated with UNCERTAIN data quality due to a few glitches and weak artefacts present in a small part of the band.

Yoon et al. (2025) found that, as expected for an absorption-line search, the peak optical depth increases at lower flux densities due to the detection limit. We see this with the two detections as well as with the peak optical depth upper limits in Figure 5. The two detections in this figure are visually well above the detection limit, and the 150 mJy bright-source sample limit. Additionally, the mean value of the peak optical depth for the two detections is 0.099, which is greater than the median value of τ_{pk} = 0.030 obtained in the sample of 136 lines compiled by Curran (2021).

7.2 Radio spectral index

Most extragalactic radio sources found in surveys at ASKAP frequencies have well-defined power law spectra, with a mean spectral index of -0.75 and dispersion of 0.2 (e.g. Kellermann & Owen, 1988). Sources with a spectral index $\gtrsim -0.5$ are usually part of the flat-spectrum population. This work focuses on the subset of sources with compact components identified by their IPS. Sources dominated by compact structure have

https://doi.org/10.1017/pasa.2026.10238 Published online by Cambridge University Press

much more complex SEDs, and a figure of the spectral index and NSI of sources can help classify different populations of sources. Radio sources with compact hot spots in their lobes which are only a small fraction of the total flux density, have a low NSI with power law spectral index $\alpha \sim -0.7$. CSS sources have a high NSI with a similar steep power law spectral index, while PS and flat-spectrum sources all have a mid to high NSI as seen in Figure 7 and Chhetri et al. (2026).

The two-point radio spectral index α of a source, where the flux density is S_1 at frequency ν_1 and S_2 at ν_2 is:

$$\alpha = \frac{\log(S_1/S_2)}{\log(\nu_1/\nu_2)}$$

The sources in the ASKAP IPS catalogue were observed at 820 MHz and also by MWA IPS at 162 MHz. The compact flux densities from both catalogues were used to characterise the spectral index of the compact component between 162 and 820 MHz. The compact flux density was obtained by multiplying the peak flux density by the NSI. The flux density measurements however were taken from RACS-low, which was made at a slightly different frequency, so there is a flux density error of a few percent at 820 MHz. We emphasise that the spectral index in this work is for the compact scintillating component of the source, while the SED model fitting uses the flux densities for the total source. However, for sources with a high NSI (compact sources), the compact flux density and the total flux density are the same.

Figure 7 shows the ASKAP NSI and MWA NSI vs the two-point spectral index of the compact scintillating component for all of the sources in the sample. There were 92 sources which had both an ASKAP NSI and an MWA NSI, and therefore a measurement of the spectral index. The sources with only NSI upper limits have no detectable compact component, and so they were not included here. The sources classified as peaked from their radio SED fits are shown by the orange circles, and the two sources found to have H I absorption in their spectra are shown by the black stars. The H I absorption sources are part of the PS sources group. Power law sources are shown by the grey circles, and flat or inverted sources are shown by the blue triangles.

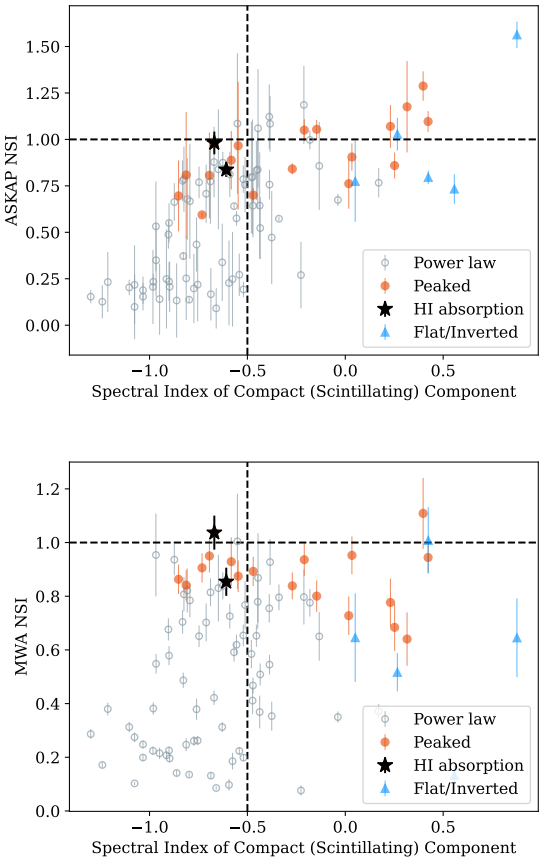


Figure 7. On the top: the ASKAP NSI vs. the spectral index of the compact scintillating component for all of the sources in the final catalogue shown by the grey circles. The peaked sources are shown by the orange triangles, and the two sources that had H I absorption observed in their spectra are shown by the black stars. On the bottom: the MWA NSI vs. spectral index. The spectral index has been calculated between MWA 162 MHz and ASKAP 820 MHz.

7.3 Median NSI values for galaxies and quasars

Since the optical identifications for the bright-source sample are incomplete, and quasars are likely to be over-represented among the identified sources, we need to be cautious in making general statements about the statistics of the quasar and galaxy populations.

However, we can compare the NSI values of confirmed galaxies and quasars in Tables 9 and 10, noting that the ASKAP NSI value represents the fraction of flux density arising from a component less than 0.1 arcsec in size. Table 8 shows the results.

As can be seen from Table 8, there is a significant difference between the NSI medians for the galaxies and quasars. This could be because there are some blazars in our sample such as the uncommon source discussed below, which most likely

Table 8. Median values of NSI for optically-identified galaxies and quasars in the bright-source (> 150 mJy) sample. The listed median redshifts for the galaxies and quasars are based mainly on photometric redshift estimates. Most of the 'Unclassified' objects are expected to be galaxies with extended radio emission.

Type	Number	Redshift median	NSI median
Galaxies	33	1.03 ± 0.16	0.30 ± 0.07
Quasars	20	1.42 ± 0.20	0.69 ± 0.11
Unclassified	26	..	0.22 ± 0.07

https://doi.org/10.1017/pasa.2026.10238 Published online by Cambridge University Press

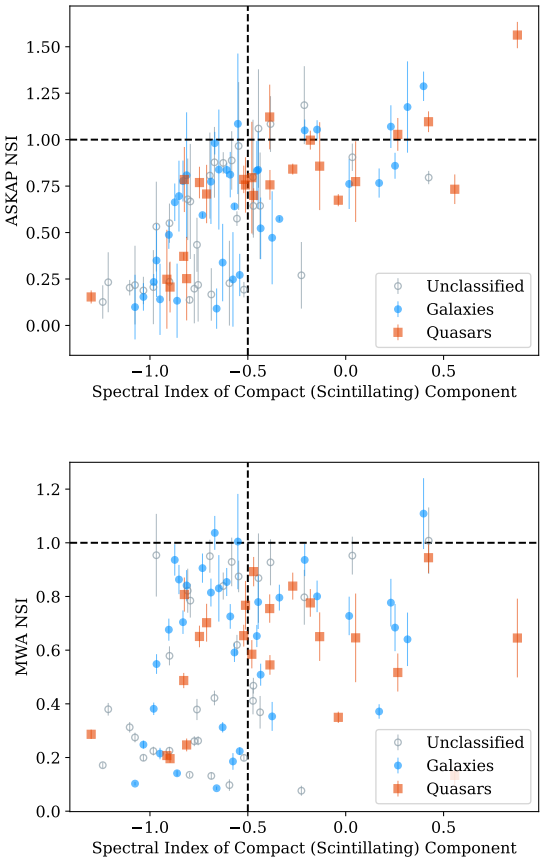


Figure 8. On the top: the ASKAP NSI vs. the spectral index of the compact scintillating component for all of the sources in the final catalogue, including sources classified as either galaxies or quasars using a photometric classification and/or a spectroscopic classification. On the bottom: the MWA NSI vs. spectral index. Galaxies are shown by blue circles and quasars are shown by orange squares. As in Figure 7, the spectral index has been calculated between MWA 162 MHz and ASKAP 820 MHz.

have SEDs classified as flat/inverted. Blazars differ from quasars because their jet axis is closely aligned to our line of sight, causing relativistic beaming (Giroletti et al., 2016). Chhetri et al. (2018) find that the high-frequency (20 GHz) radio emission of blazars is often dominated by a compact radio core, and at lower frequencies (162 MHz), the emission is dominated by the extended structure which has been built up by the AGN activity over a long period of time. From Table 8 and Figure 8, we see that the low NSI values are very similar for galaxies and unclassified sources. This provides strong evidence that the unclassified sources are more distant galaxies, and being more distant means higher radio luminosity, which is consistent with the suggestion by Chhetri et al. (2026) that these are FRII sources with a small fraction of their flux density in scintillating hotspots.

7.4 The uncommon source NVSS J215031-223200

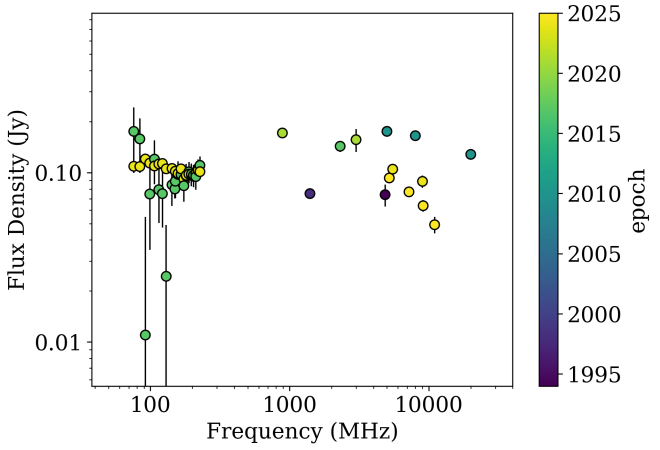


Figure 9. Radio SED of NVSS J215031-223200, showing high-frequency variability.

NVSS J215031-223200 was identified by eye as an outlier in terms of both compact-component spectral index and ASKAP NSI in Figure 7, with an ASKAP NSI of 1.56 ± 0.07. It is classified as a flat-spectrum radio source by Healey et al. 2007, and its SED is presented in Figure 9. RadioSED prefers a PS model, and this preference is due to the large scatter in high frequency flux densities, which is the result of variability over the $\sim$ 20 yr span of observations. However, even this best-fit model is a poor characterisation of the broadband SED, since RadioSED does not account for source variability in fitting, and we stress that this is not a true PS source.

NVSS J215031-223200 is classified as a quasar, with a spectroscopic redshift of 2.113 ± 0.638 from the Gaia-unWISE quasar catalogue (Quaia; Storey-Fisher et al., 2024), but the radio variability of the source suggests that it is likely a blazar. The SEDs of blazars are usually strongly affected by relativistic beaming, while PS sources are not expected to show strong variability.

Recent observations with the Australia Telescope Compact Array (ATCA) at $4 - 12$ GHz, shown in Figure 9, reveal that this source has varied by a factor of ~ 3 over the course

https://doi.org/10.1017/pasa.2026.10238 Published online by Cambridge University Press

of 12 months between initial monitoring in December 2024 (ATCA project C3664), and subsequent follow up (ATCA project C3550) in December 2025. This high degree of variability is likely present down to at least ASKAP frequencies, based on the factor of ~ 2.5 difference between RACS-low (888 MHz) and NVSS (1.4 GHz), although repeat observations by the MWA between 2013 and 2020 show the radio flux density is stable below 300 MHz to within the instrument uncertainties.

This absence of radio variability at low frequencies is characteristic of flat-spectrum radio quasars (Ciaramella et al., 2004). It is interesting to note that the NSI of this source also decreases dramatically at MWA wavelengths (NSI(MWA) = 0.65 ± 0.15), which is most likely due to an extended steep spectrum structure becoming increasingly dominant at lower frequencies. This also causes the upturn in the SED in Figure 9 below 100 MHz. This source has no observed H I absorption, and it also did not have a tentative detection. Its integrated flux density is just above the 150 mJy bright-source sample limit, and it is located along the trend in the integrated flux density-peak optical depth diagram in Figure 5.

8. SUMMARY

A search in the first ASKAP interplanetary scintillation field for H I absorption using FLASH has resulted in two detections in J212805.5-232946 (MRC 2125-237) and J213437.6-23553 (MRC 2131-241) without optical preselection. Both of these detections were strong lines with high Bayesian evidence values ln (B). The short 2.5 minute observation of this field demonstrates the extraordinary efficiency of the IPS method for finding many thousands of compact sources with matches in the full FLASH survey. With these IPS observations at a similar frequency to FLASH, we were able to investigate the sub-arcsec structure of sources in the field. SED fitting in this field has affirmed that most peaked-spectrum (PS) sources are compact sources, and has shown that both H I absorption detections have peaked SEDs. In future, SEDs could be created using data spanning different frequencies, particularly in the $\sim 300 - 700$ MHz range, which could be achieved with the upcoming SKA, allowing for better constrained fits. The spectroscopic redshift for the source J212805.5-232946 matched the H I absorption line redshift (0.95). J212805.5-232946 also has a broad H I absorption line which, in combination with its optical redshift, points to it being an associated source. On the other hand, J213437.6-235537 has a narrow absorption line which suggests it is an intervening source. Both of these sources were classified as galaxies. There was an uncommon source identified as being an outlier in compact spectral index, with a very high ASKAP NSI, as well as having large scatter in flux density at higher frequencies. We anticipate that since it is feasible to carry out many more IPS observations using ASKAP and MWA, this technique can be used to assist with identifying candidates for H I absorption in large spectral-line datasets such as the full FLASH survey. In these large datasets, compact sources can be easily identified, and PS sources and H I absorption can be identified from a much smaller sample. Our results also indicate that IPS may not only be linked to compact sources but to PS sources as well, demonstrating that IPS is a promising tool for current and future HI absorption studies.

Acknowledgement

The authors would like to thank Roberto Soria and Stas Shabala for providing useful comments which improved the clarity of this paper. This scientific work uses data obtained from Inyarrimanha Ilgari Bundara / the Murchison Radio-astronomy Observatory. We acknowledge the Wajarri Yamaji People as the Traditional Owners and native title holders of the Observatory site. CSIRO's ASKAP radio telescope is part of the Australia Telescope National Facility (https://ror.org/05qajvd42). Operation of ASKAP is funded by the Australian Government with support from the National Collaborative Research Infrastructure Strategy. ASKAP uses the resources of the Pawsey Supercomputing Research Centre. Establishment of ASKAP, Inyarrimanha Ilgari Bundara, the CSIRO Murchison Radioastronomy Observatory and the Pawsey Supercomputing Research Centre are initiatives of the Australian Government, with support from the Government of Western Australia and the Science and Industry Endowment Fund.

The Legacy Surveys consist of three individual and complementary projects: the Dark Energy Camera Legacy Survey (DECaLS; Proposal ID #2014B-0404; PIs: David Schlegel and Arjun Dey), the Beijing-Arizona Sky Survey (BASS; NOAO Prop. ID #2015A-0801; PIs: Zhou Xu and Xiaohui Fan), and the Mayall z-band Legacy Survey (MzLS; Prop. ID #2016A-0453; PI: Arjun Dey). DECaLS, BASS and MzLS together include data obtained, respectively, at the Blanco telescope, Cerro Tololo Inter-American Observatory, NSF's NOIRLab; the Bok telescope, Steward Observatory, University of Arizona; and the Mayall telescope, Kitt Peak National Observatory, NOIRLab. Pipeline processing and analyses of the data were supported by NOIRLab and the Lawrence Berkeley National Laboratory (LBNL). The Legacy Surveys project is honored to be permitted to conduct astronomical research on Iolkam Du'ag (Kitt Peak), a mountain with particular significance to the Tohono O'odham Nation.

NOIRLab is operated by the Association of Universities for Research in Astronomy (AURA) under a cooperative agreement with the National Science Foundation. LBNL is managed by the Regents of the University of California under contract to the U.S. Department of Energy.

This project used data obtained with the Dark Energy Camera (DECam), which was constructed by the Dark Energy Survey (DES) collaboration. Funding for the DES Projects has been provided by the U.S. Department of Energy, the U.S. National Science Foundation, the Ministry of Science and Education of Spain, the Science and Technology Facilities Council of the United Kingdom, the Higher Education Funding Council for England, the National Center for Supercomputing Applications at the University of Illinois at Urbana-Champaign, the Kavli Institute of Cosmological Physics at the University of Chicago, Center for Cosmology and Astro-Particle Physics

https://doi.org/10.1017/pasa.2026.10238 Published online by Cambridge University Press

at the Ohio State University, the Mitchell Institute for Fundamental Physics and Astronomy at Texas A&M University, Financiadora de Estudos e Projetos, Fundacao Carlos Chagas Filho de Amparo, Financiadora de Estudos e Projetos, Fundacao Carlos Chagas Filho de Amparo a Pesquisa do Estado do Rio de Janeiro, Conselho Nacional de Desenvolvimento Cientifico e Tecnologico and the Ministerio da Ciencia, Tecnologia e Inovacao, the Deutsche Forschungsgemeinschaft and the Collaborating Institutions in the Dark Energy Survey. The Collaborating Institutions are Argonne National Laboratory, the University of California at Santa Cruz, the University of Cambridge, Centro de Investigaciones Energeticas, Medioambientales y Tecnologicas-Madrid, the University of Chicago, University College London, the DES-Brazil Consortium, the University of Edinburgh, the Eidgenossische Technische Hochschule (ETH) Zurich, Fermi National Accelerator Laboratory, the University of Illinois at Urbana-Champaign, the Institut de Ciencies de l'Espai (IEEC/CSIC), the Institut de Fisica d'Altes Energies, Lawrence Berkeley National Laboratory, the Ludwig Maximilians Universitat Munchen and the associated Excellence Cluster Universe, the University of Michigan, NSF's NOIRLab, the University of Nottingham, the Ohio State University, the University of Pennsylvania, the University of Portsmouth, SLAC National Accelerator Laboratory, Stanford University, the University of Sussex, and Texas A&M University.

BASS is a key project of the Telescope Access Program (TAP), which has been funded by the National Astronomical Observatories of China, the Chinese Academy of Sciences (the Strategic Priority Research Program "The Emergence of Cosmological Structures" Grant # XDB09000000), and the Special Fund for Astronomy from the Ministry of Finance. The BASS is also supported by the External Cooperation Program of Chinese Academy of Sciences (Grant # 114A11KYSB20160057), and Chinese National Natural Science Foundation (Grant # 12120101003, # 11433005).

The Legacy Survey team makes use of data products from the Near-Earth Object Wide-field Infrared Survey Explorer (NEOWISE), which is a project of the Jet Propulsion Laboratory/California Institute of Technology. NEOWISE is funded by the National Aeronautics and Space Administration.

The Legacy Surveys imaging of the DESI footprint is supported by the Director, Office of Science, Office of High Energy Physics of the U.S. Department of Energy under Contract No. DE-AC02-05CH1123, by the National Energy Research Scientific Computing Center, a DOE Office of Science User Facility under the same contract; and by the U.S. National Science Foundation, Division of Astronomical Sciences under Contract No. AST-0950945 to NOAO.

The Photometric Redshifts for the Legacy Surveys (PRLS) catalog used in this paper was produced thanks to funding from the U.S. Department of Energy Office of Science, Office of High Energy Physics via grant DE-SC0007914.

This research was supported by an Australian Government Research Training Program (RTP) Scholarship. HY is supported by the National Research Foundation of Korea (NRF) grant funded by the Korea government (MSIT, RS-2025-00516062), and by funding from Korean government (Korea AeroSpace Administration (KASA), grant number RS-2026-25587698). This research has made use of NASA's Astrophysics Data System Bibliographic Services, the NASA/IPAC Extragalactic Database (NED) which is funded by the National Aeronautics and Space Administration and operated by the California Institute of Technology and the crossmatch service provided by CDS, Strasbourg.

We made use of Astropy (Astropy Collaboration et al., 2013, 2018, 2022), Matplotlib (Hunter, 2007), NumPy (Harris et al., 2020), and pandas (Wes McKinney, 2010). For the `RadioSED` code, a full list of modules and packages used is available on GitHub.

9. DATA AVAILABILITY

Archived data from ASKAP surveys, such as FLASH, can be obtained through the CSIRO ASKAP Science Data Archive, CASDA (http://data.csiro.au/). Other survey data used in SED construction and multiwavelength analysis is available through the CDS VizieR catalogue service. Measurements derived from the ASKAP-MWA IPS catalogue are available in the companion paper Chhetri et al. (2026) and in the Appendix of this paper. Any additional data is available upon reasonable request to the corresponding author.

References

Aditya, J. N. H. S., Yoon, H., Allison, J. R., et al. 2024, MNRAS, 527, 8511

Allison, J. R., Sadler, E. M., Mahony, E. K., Moss, V. A., & Yoon, H. 2021, Astronomische Nachrichten, 342, 1062

Allison, J. R., Sadler, E. M., & Whiting, M. T. 2012, PASA, 29, 221

Allison, J. R., Sadler, E. M., Bellstedt, S., et al. 2020, MNRAS, 494, 3627

Allison, J. R., Sadler, E. M., Amaral, A. D., et al. 2022, PASA, 39, e010

Astropy Collaboration, Robitaille, T. P., Tollerud, E. J., et al. 2013, A&A, 558, A33

Astropy Collaboration, Price-Whelan, A. M., Sipőcz, B. M., et al. 2018, AJ, 156, 123

Astropy Collaboration, Price-Whelan, A. M., Lim, P. L., et al. 2022, ApJ, 935, 167

Baker, J. C., Hunstead, R. W., Kapahi, V. K., & Subrahmanya, C. R. 1999, ApJS, 122, 29

Best, P. N., Kauffmann, G., Heckman, T. M., & Ivezić, Ž. 2005, MNRAS, 362, 9

Burbidge, E. M. 1970, ApJ, 160, L33

Callingham, J. R., Ekers, R. D., Gaensler, B. M., et al. 2017, ApJ, 836, 174

Chandola, Y., Sirothia, S. K., & Saikia, D. J. 2011, MNRAS, 418, 1787

Chhetri, R., Morgan, J., Ekers, R. D., et al. 2018, MNRAS, 474, 4937

Chhetri, R., Morgan, J. S., Ekers, R. D., et al. 2026, First results of sub-arcsecond scale objects identified with ASKAP using interplanetary scintillation, arXiv:2606.28302 [astro-ph.CO]

Chhetri, R., Morgan, J., Moss, V., et al. 2023, Advances in Space Research, 72, 5361

Ching, J. H. Y., Sadler, E. M., Croom, S. M., et al. 2017, MNRAS, 464, 1306

Ciaramella, A., Bongardo, C., Aller, H. D., et al. 2004, A&A, 419, 485

Clarke, M. 1964, PhD Thesis, Cambridge University

Condon, J. J., Cotton, W. D., Greisen, E. W., et al. 1998, AJ, 115, 1693

Curran, S. J. 2021, MNRAS, 506, 1548

Curran, S. J., Whiting, M. T., Sadler, E. M., & Bignell, C. 2013, MNRAS, 428, 2053

Dallacasa, D., Stanghellini, C., Centonza, M., & Fanti, R. 2000, A&A, 363, 887

https://doi.org/10.1017/pasa.2026.10238 Published online by Cambridge University Press

Dey, A., Schlegel, D. J., Lang, D., et al. 2019a, AJ, 157, 168
—. 2019b, AJ, 157, 168
Drinkwater, M. J., Webster, R. L., Francis, P. J., et al. 1997, MNRAS, 284, 85
Dunlop, J. S., Peacock, J. A., Savage, A., et al. 1989, MNRAS, 238, 1171
Geréb, K., Maccagni, F. M., Morganti, R., & Oosterloo, T. A. 2015, A&A, 575, A44
Giroletti, M., D'Ammando, F., Orienti, M., Lico, R., & Collaboration, T. F.-L. 2016, Galaxies, 4
Glowacki, M., Allison, J. R., Moss, V. A., et al. 2019, MNRAS, 489, 4926
Gupta, N., Salter, C. J., Saikia, D. J., Ghosh, T., & Jeyakumar, S. 2006, MNRAS, 373, 972
Hale, C. L., McConnell, D., Thomson, A. J. M., et al. 2021, PASA, 38, e058
Hancock, P. J., Trott, C. M., & Hurley-Walker, N. 2018, PASA, 35, e011
Harris, C. R., Millman, K. J., van der Walt, S. J., et al. 2020, Nature, 585, 357
Healey, S. E., Romani, R. W., Taylor, G. B., et al. 2007, ApJS, 171, 61
Heckman, T. M., & Best, P. N. 2014, ARA&A, 52, 589
Hewish, A., Scott, P. F., & Wills, D. 1964, Nature, 203, 1214
Hewish, A., & Symonds, M. D. 1969, Planet. Space Sci., 17, 313
Holt, J., Tadhunter, C. N., & Morganti, R. 2008, MNRAS, 387, 639
Hotan, A. W., Bunton, J. D., Chippendale, A. P., et al. 2021, PASA, 38, e009
Hunter, J. D. 2007, Computing in Science & Engineering, 9, 90
Hurley-Walker, N., Galvin, T. J., Duchesne, S. W., et al. 2022, PASA, 39, e035
Kapahi, V. K., Athreya, R. M., van Breugel, W., McCarthy, P. J., & Subrahmanya, C. R. 1998, ApJS, 118, 275
Kellermann, K. I., & Owen, F. N. 1988, in Galactic and Extragalactic Radio Astronomy, ed. K. I. Kellermann & G. L. Verschuur, 563
Kerrison, E. F., Allison, J. R., Moss, V. A., Sadler, E. M., & Rees, G. A. 2024, MNRAS, 533, 4248
Kerrison, E. F., Sadler, E. M., Moss, V. A., et al. 2025, MNRAS, 543, 3895
Lacy, M., Baum, S. A., Chandler, C. J., et al. 2020, PASP, 132, 035001
Maccagni, F. M., Morganti, R., Oosterloo, T. A., Geréb, K., & Maddox, N. 2017, A&A, 604, A43
Mahony, E. K., Allison, J. R., Sadler, E. M., et al. 2022, MNRAS, 509, 1690
McCarthy, P. J., Kapahi, V. K., van Breugel, W., et al. 1996, ApJS, 107, 19
McConnell, D., Hale, C. L., Lenc, E., et al. 2020, Publications of the Astronomical Society of Australia, 37, e048
Morgan, J. S., Macquart, J.-P., Chhetri, R., et al. 2019, PASA, 36, e002
Morgan, J. S., Macquart, J. P., Ekers, R., et al. 2018, MNRAS, 473, 2965
Morganti, R., & Oosterloo, T. 2018, A&A Rev., 26, 4
Murphy, T., Sadler, E. M., Ekers, R. D., et al. 2010, MNRAS, 402, 2403
O'Dea, C. P. 1998, PASP, 110, 493
O'Dea, C. P., & Saikia, D. J. 2021, A&A Rev., 29, 3
Orienti, M., Dallacasa, D., & Stanghellini, C. 2007, A&A, 461, 923
Owen, F. N., Ledlow, M. J., & Keel, W. C. 1995, AJ, 109, 14
Péroux, C., & Howk, J. C. 2020, ARA&A, 58, 363
Peterson, B. A., Wright, A. E., Jauncey, D. L., & Condon, J. J. 1979, ApJ, 232, 400
Pihlström, Y. M., Conway, J. E., & Vermeulen, R. C. 2003, A&A, 404, 871
Planck Collaboration, Aghanim, N., Akrami, Y., et al. 2020, A&A, 641, A6
Rickett, B. J. 1973, J. Geophys. Res., 78, 1543
Roster, W., Salvato, M., Krippendorf, S., et al. 2024, A&A, 692, A260
Roster, W., Sadler, E., Mahony, E., et al. 2026, PASA, 43, e065
Sadler, E. M., Chhetri, R., Morgan, J., et al. 2019, MNRAS, 483, 1354
Sadler, E. M., Moss, V. A., Allison, J. R., et al. 2020, MNRAS, 499, 4293
Saxena, A., Salvato, M., Roster, W., et al. 2024, A&A, 690, A365
Skilling, J. 2004, in American Institute of Physics Conference Series, Vol. 735, Bayesian Inference and Maximum Entropy Methods in Science and Engineering: 24th International Workshop on Bayesian Inference and Maximum Entropy Methods in Science and Engineering, ed. R. Fischer, R. Preuss, & U. V. Toussaint, 395
Slob, M. M., Callingham, J. R., Röttgering, H. J. A., et al. 2022, Astronomy & Astrophysics, 668, A186
Snellen, I. A. G., Schilizzi, R. T., de Bruyn, A. G., et al. 1998, A&AS, 131, 435
Storey-Fisher, K., Hogg, D. W., Rix, H.-W., et al. 2024, ApJ, 964, 69
Su, R., Sadler, E. M., Allison, J. R., et al. 2022a, MNRAS, 516, 2947
—. 2022b, MNRAS, 516, 2947
Tingay, S. J., Goeke, R., Bowman, J. D., et al. 2013, PASA, 30, e007
Titov, O., Jauncey, D. L., Johnston, H. M., Hunstead, R. W., & Christensen, L. 2011, AJ, 142, 165
Vermeulen, R. C., Pihlström, Y. M., Tschager, W., et al. 2003, A&A, 404, 861
Véron-Cetty, M. P., Woltjer, L., Staveley-Smith, L., & Ekers, R. D. 2000, A&A, 362, 426
Wang, Z., Bannister, K. W., Gupta, V., et al. 2025, PASA, 42, e005
Wes McKinney. 2010, in Proceedings of the 9th Python in Science Conference, ed. Stéfan van der Walt & Jarrod Millman, 56
Whiting, M., & Humphreys, B. 2012, PASA, 29, 371
Yoon, H., Sadler, E. M., Mahony, E. K., et al. 2025, PASA, 42, e088

Appendix 1. Data table

https://doi.org/10.1017/pasa.2026.10238 Published online by Cambridge University Press

https://doi.org/10.1017/pasa.2026.10238 Published online by Cambridge University Press

Table 9. Bright-source sample

Source	NED name	RAdeg	DEdeg	Object Type	F_tot	F_pk	S/N	z_phot	z_spec	err	z_ref	NSI	err	NSI	err	SED
		J2000		(LS 10)	(mJy)	(mJy)	Cont	PICZL		z_spec		ASKAP	NSI	MWA	NSI	
J212805.5-232944	MRC 2125-237	322.022934	-23.495761	Galaxy	1114.88	1093.66	49.36	..	0.95	0.05	Mc96	0.98	0.06	1.04	0.06	PS
J212857.5-224244	NVSS J212857-224245	322.239795	-22.712374	Galaxy	239.37	232.78	26.86	1.5	..	..	..	< 0.18	..	0.38	0.02	PL
J212937.1-224828	MRC 2126-230	322.404881	-22.807968	..	1301.06	769.16	106.69	..	..	..	..	0.13	0.09	0.17	0.01	PL
J213153.3-221102	NVSS J213153-221103	322.972376	-22.184104	..	164.29	150.42	51.72	..	..	..	..	< 0.11	..	0.15	0.04	PL
J213154.3-230827	NVSS J213154-230828	322.976505	-23.140914	Quasar	162.07	153.57	43.72	..	1.484	0.088	Quaia	< 0.16	..	0.20	0.02	PL
J213250.4-230232	MRC 2129-232	323.210089	-23.042455	..	477.5	252.83	65.9	..	..	..	..	< 0.07	..	< 0.00	< 0.02	PL
J213334.2-213818	NVSS J213334-213818	323.392862	-21.638441	Quasar	276.24	271.67	80.54	0.1	..	..	..	0.7	0.04	0.89	0.05	PS
J213339.0-234916	NVSS J213339-234917	323.412796	-23.821358	Galaxy	207.1	198.8	45.27	1.18	..	..	..	< 0.18	..	0.38	0.02	PL
J213411.6-173542	PKS 2131-178	323.548689	-17.595065	Galaxy	332.38	323.23	22.15	0.56	..	..	..	0.66	0.1	0.94	0.06	PL
J213429.3-244308	NVSS J213429-244309	323.62245	-24.719154	Quasar	303.28	241.04	25.34	1.15	..	..	..	< 0.55	..	0.25	0.02	PL
J213437.6-235535	MRC 2131-241	323.656723	-23.926639	Galaxy	554.65	533.23	113.29	0.66	..	..	..	0.84	0.04	0.85	0.05	PS
J213516.8-173429	PKS 2132-177	323.820021	-17.574727	..	1585.87	1142.84	104.13	..	..	..	..	0.2	0.04	0.31	0.02	PL
J213729.4-195327	NVSS J213729-195326	324.37281	-19.89097	..	261.48	239.2	74.7	..	..	..	..	0.17	0.14	0.13	0.01	PL
J213749.9-204232	PKS 2135-20	324.458263	-20.709059	Galaxy	5223.87	5076.27	552.18	0.55	0.635	0.001	Ho08	0.59	0.01	0.91	0.05	PS
J213801.0-253148	MRC 2135-257	324.504382	-25.530162	Galaxy	819	801.79	61.81	..	1.31	0.05	Mc96	0.83	0.16	0.65	0.04	PL
J213802.1-221823	NVSS J213802-221824	324.508853	-22.306561	Quasar	180.82	169.62	98.22	0.2	..	..	..	0.21	0.14	0.20	0.01	PL
J213805.0-184330	PKS 2135-18	324.521035	-18.725081	..	2225.38	1894.2	351.16	..	..	..	..	0.14	0.02	0.14	0.01	PL
J213837.1-243954	PKS 2135-248	324.65472	-24.665006	Quasar	405.41	394.64	135.97	0.62	0.819	0.001	Pe79	1.14	0.04	..	..	PS
J213838.3-175040	MRC 2135-180	324.659658	-17.844705	..	597.32	578.81	79.52	..	..	..	..	0.57	0.04	0.62	0.04	PL
J213841.9-181045	PKS 2135-184	324.674769	-18.179252	Galaxy	2402.56	2353.56	293.25	0.1	0.1887	0.0001	Ow95	0.57	0.01	0.80	0.05	PL
J213847.4-184931	NVSS J213847-184930	324.697736	-18.825485	..	399.1	388.94	76.27	..	..	..	..	0.8	0.04	1.01	0.12	I
J213857.0-195725	NVSS J213857-195723	324.737765	-19.957044	..	226.11	219.2	59.26	..	..	..	..	0.87	0.06	0.84	0.05	PL
J213908.5-245718	NVSS J213908-245718	324.785738	-24.955083	..	232.76	225.97	50.98	..	..	..	..	0.64	0.17	0.47	0.03	PL
J213913.1-245414	MRC 2136-251	324.804976	-24.904024	Galaxy	729.56	697.9	162.31	0.6	0.939	..	Ba99	0.27	0.11	0.22	0.01	PL
J213924.5-255643	MRC 2136-261	324.852211	-25.945518	..	1540.24	888.59	55.53	..	..	..	..	0.88	0.19	0.42	0.03	PL
J213926.4-172352	NVSS J213926-172351	324.860129	-17.397855	..	240.84	234.84	38.44	..	..	..	..	0.91	0.07	0.95	0.07	PS
J213939.5-183810	MRC 2136-188	324.914888	-18.636148	..	823.17	796.25	142.44	..	..	..	..	0.19	0.04	0.20	0.01	PL
J213945.0-250114	NVSS J213945-250115	324.93767	-25.0208	Galaxy	214.09	197.02	44.38	1.58	..	..	..	< 0.30	..	0.19	0.02	PL
J213950.9-191630	NVSS J213951-191629	324.96239	-19.275152	..	274.56	173.92	32.94	..	..	..	..	0.27	0.18	0.08	0.02	PL
J213957.7-212034	NVSS J213957-212034	324.99066	-21.342938	..	207.03	165	48.32	..	..	..	..	0.22	0.21	0.27	0.02	PL

https://doi.org/10.1017/pasa.2026.10238 Published online by Cambridge University Press

Source	NED name	RAdeg	DEdeg	Object Type	F_tot	F_pk	S/N	z_phot	z_spec	err	z_ref	NSI	err	NSI	err	SED
		J2000		(LS 10)	(mJy)	(mJy)	Cont	PICZL		z_spec		ASKAP	NSI	MWA	NSI	
J214010.7-161628	MRC 2137-165	325.044656	-16.274532	..	1193.14	566.08	27.9	..	..	..	..	< 0.21	..	0.09	0.01	PL
J214011.6-182529	NVSS J214011-182528	325.048503	-18.424837	..	194.34	187.38	38.17	..	..	..	..	0.23	0.16	0.38	0.02	PL
J214032.5-211559	NVSS J214032-211559	325.135587	-21.266663	..	316.24	250.32	93.7	..	..	..	..	0.24	0.1	0.23	0.01	PL
J214119.6-204102	NVSS J214119-204102	325.331842	-20.684099	..	197.22	182.79	63.3	..	..	..	..	< 0.11	..	0.14	0.02	PL
J214159.8-254757	NVSS J214159-254758	325.499304	-25.799395	..	254.44	213.4	34.33		..	..	..	< 0.61	..	0.13	0.01	PL
J214201.7-191401	NVSS J214201-191400	325.507319	-19.233788	Quasar	362.74	352.25	112.49	1.82	..	..	..	0.84	0.03	0.84	0.05	PS
J214204.5-232919	NVSS J214204-232920	325.519116	-23.488684	Galaxy	280.62	265.93	167.41	1.14	..	..	..	0.13	0.2	0.14	0.01	PL
J214212.9-180743	NVSS J214212-180742	325.553896	-18.128764	Galaxy	206.05	192.92	41.41	1.66	..	..	..	< 0.10	..	0.21	0.02	PL
J214230.8-244438	NVSS J214230-244440	325.628434	-24.744064	Quasar	251.71	221.22	111.98	0.58	0.833	..	deWitt23	0.73	0.08	0.13	0.04	I
J214233.3-241231	NVSS J214233-241232	325.638763	-24.208714	Galaxy	259.09	220.28	114.65	0.63	..	..	..	< 0.10	..	< 0.05	< 0.02	PL
J214236.9-180620	NVSS J214236-180619	325.653883	-18.105705	..	169.43	160.9	32.5	..	..	..	..	0.21	0.2	0.22	0.02	PL
J214241.9-230337	NVSS J214241-230340	325.674633	-23.060547	Quasar	175.3	171.6	104.72	0.31	..	..	..	1	0.05	0.78	0.05	PL
J214304.2-164147	NVSS J214304-164146	325.767726	-16.696639	Galaxy	255.26	250.01	24.7	1.09	..	..	..	0.76	0.13	0.73	0.07	PS
J214307.4-183553	MRC 2140-188	325.78102	-18.598324	Galaxy	551.49	533.79	167.47	0.15	0.1873	0.0002	Ow95	0.23	0.04	0.38	0.02	PL
J214329.1-181100	MRC 2140-184	325.871374	-18.183392	Quasar	1230.97	1104.38	256.2	1.64	..	..	..	0.15	0.04	0.29	0.02	PL
J214408.8-244240	NVSS J214408-244241	326.036783	-24.711146	Quasar	172.67	163.73	72.05	1.33	..	..	..	< 0.17	..	< 0.04	< 0.05	PL
J214431.7-240210	NVSS J214431-240211	326.132174	-24.036154	..	315.54	245.53	137.65	..	..	..	..	0.2	0.19	0.26	0.02	PL
J214449.1-221552	NVSS J214449-221552	326.204797	-22.264564	Galaxy	200.36	197	127.22	0.54	..	..	..	0.49	0.08	0.68	0.04	PL
J214525.5-194841	NVSS J214525-194842	326.35641	-19.811429	Galaxy	225.08	172.67	100.3	1.55	..	..	..	0.14	0.19	0.21	0.02	PL
J214548.9-182600	NVSS J214549-182559	326.454069	-18.43357	Galaxy	183.58	179.71	59.89	1.19	..	..	..	0.86	0.07	0.68	0.09	PS
J214641.5-242957	NVSS J214641-242957	326.673226	-24.499255	..	249.59	241.99	120.51	..	..	..	..	0.55	0.11	0.58	0.04	PL
J214703.2-174012	PKS 2144-17	326.763378	-17.670175	Quasar	1566.25	1527.43	284.52	0.67	0.684	..	Bu70	0.37	0.02	0.49	0.03	PL
J214717.4-194647	NVSS J214717-194646	326.822803	-19.77975	..	246.4	222.78	90.59	..	..	..	..	0.23	0.23	< 0.00	< 0.06	PL
J214740.7-232341	MRC 2144-236	326.919624	-23.394978	Galaxy	578.85	493.93	255.16	1.34	..	..	..	0.1	0.17	0.10	0.01	PL
J214809.0-251611	NVSS J214809-251612	327.03756	-25.26982	..	305.18	272.43	62.9	..	..	..	..	< 0.34	..	0.14	0.01	PL
J214827.6-194126	MRC 2145-199	327.115112	-19.690663	Galaxy	668.15	610.56	196.18	0.8	..	..	..	0.09	0.11	0.09	0.01	PL
J214836.7-172344	PKS 2145-17	327.153103	-17.395775	Quasar	952.37	920.01	140.24	1.58	2.13	..	Dr97	0.67	0.03	0.35	0.02	PL
J214941.7-191226	MRC 2146-194	327.423955	-19.207341	Galaxy	802.07	669.19	202.44	1.01	..	..	..	0.15	0.07	0.25	0.01	PL
J215002.8-174537	NVSS J215002-174537	327.511845	-17.760509	Galaxy	331.48	321.23	70.15	0.64	..	..	..	0.77	0.08	0.37	0.03	PL
J215031.1-220820	NVSS J215031-220820	327.629643	-22.138931	Galaxy	158.81	157.03	95.3	1.41	..	..	..	< 0.15	..	0.27	0.02	PL

https://doi.org/10.1017/pasa.2026.10238 Published online by Cambridge University Press

Source	NED name	RAdeg	DEdeg	Object Type	F_tot	F_pk	S/N	z_phot	z_spec	err	z_ref	NSI	err	NSI	err	SED
		J2000		(LS 10)	(mJy)	(mJy)	Cont	PICZL		z_spec		ASKAP	NSI	MWA	NSI	
J215031.1-223200	NVSS J215031-223200	327.629708	-22.533454	Quasar	171.19	169.88	80.74	1.7	2.113	0.638	Quaia	1.56	0.07	0.65	0.15	F
J215116.5-223647	MRC 2148-228	327.818997	-22.613062	Galaxy	616.08	447.38	254.7	..	0.85	0.05	Mc96	< 0.05	..	0.06	0.00	PL
J215150.9-194606	PKS 2149-20	327.962384	-19.768507	Galaxy	2830.53	2631.81	342.71	0.34	0.424	..	Ba99	0.64	0.02	0.59	0.04	PL
J215255.4-200103	NVSS J215255-200102	328.23124	-20.017599	Quasar	242.44	189.64	45.79	1.51	..	..	..	0.25	0.27	0.21	0.01	PL
J215343.1-200103	PKS 2150-202	328.429811	-20.01752	..	1203.51	1003.95	202.68	..	..	..	..	0.19	0.07	0.20	0.01	PL
J215445.3-213357	NVSS J215445-213356	328.689165	-21.565843	Quasar	164.62	152.42	105.21	3.97	2.561	0.401	Quaia	< 0.14	..	0.26	0.02	PL
J215449.8-213551	NVSS J215449-213550	328.707682	-21.597631	..	168.58	162.64	106.26	..	..	..	..	0.32	0.21	..	..	PL
J215513.7-213702	PKS 2152-218	328.807304	-21.617432	Quasar	158.11	152.84	90.76	0.62	0.306	..	Du89	1.03	0.09	0.52	0.07	F
J215517.3-233805	NVSS J215517-233806	328.822459	-23.634893	Galaxy	168.43	158.07	50.64	1.06	..	..	..	< 0.36	..	0.17	0.02	PL
J215607.3-183741	PKS 2153-188	329.030705	-18.62812	Galaxy	283.08	278.3	60.74	0.49	0.31	..	Du89	0.34	0.21	0.31	0.02	PL
J215729.1-180703	PKS 2154-183	329.371289	-18.117601	Quasar	1846.47	1803.57	99.99	1.08	1.423	..	Du89	1.1	0.06	0.94	0.06	PS
J215735.6-201746	PKS 2154-205	329.398686	-20.296199	Quasar	287	279.2	116.72	1.96	2.009	0.075	Quaia	0.77	0.08	0.65	0.04	PL
J215816.4-191810	PKS 2155-195	329.568462	-19.303013	..	197.14	155.18	35.56	..	..	..	..	< 0.24	..	0.12	0.02	PL
J215911.8-185830	PKS 2156-192	329.799417	-18.975096	Galaxy	274.24	244.2	30.84	0.49	..	..	..	< 0.31	..	0.29	0.02	PL
J215938.3-212743	NVSS J215938-212743	329.909795	-21.461953	Galaxy	163.54	155.6	86.5	1.27	..	..	..	< 0.23	..	0.23	0.02	PL
J215957.0-211040	PKS 2157-214	329.987885	-21.178018	..	441.7	423.58	183.96	..	..	..	..	0.22	0.2	0.26	0.02	PL
J220027.5-231117	NVSS J220027-231118	330.114667	-23.18829	Quasar	181.48	178	22.9	0.96	..	..	..	< 1.21	..	0.83	0.06	PS
J220040.2-230722	NVSS J220040-230723	330.167736	-23.122855	Galaxy	224.8	221.67	28.36	0.31	..	..	..	< 0.98	..	0.82	0.05	PL
J220041.1-185540	PKS 2157-191	330.171284	-18.928032	Galaxy	371.27	354.47	28.63	1.54	..	..	..	< 0.41	..	0.15	0.01	PL
J220051.2-220557	NVSS J220051-220557	330.213559	-22.099424	Quasar	255.72	183.57	68.3	..	1.585	0.131	Quaia	< 0.32	..	0.10	0.01	PL
J220054.6-194724	NVSS J220054-194723	330.227886	-19.790154	Galaxy	174.52	168.76	39.22	4.79	..	..	..	< 0.47	..	0.42	0.03	PL
J220127.0-202536	PKS 2158-206	330.362846	-20.426705	Quasar	523.11	509.88	173.3	1.84	2.272	..	Ba99	0.79	0.07	0.65	0.04	PL
J220150.2-211805	PKS 2159-215	330.459264	-21.301556	Galaxy	328.8	318.2	119.6	1.41	..	..	..	0.81	0.12	0.73	0.05	PL
J220212.5-190253	PKS 2159-192	330.552406	-19.048233	Galaxy	466.14	447.89	23.61	1.52	..	..	..	< 0.50	..	0.31	0.02	PL
J220217.1-201748	PKS 2159-205	330.571573	-20.296709	Galaxy	154.15	151.44	41.04	0.63	..	..	..	1.18	0.25	0.64	0.10	PS
J220241.8-195509	PKS 2159-201	330.674251	-19.919429	Galaxy	808.49	780.1	135.89	1.48	..	..	..	0.78	0.11	0.70	0.04	PL
J220245.7-214332	NVSS J220245-21433	330.690603	-21.725633	Galaxy	286.68	278.87	71.64	1.52	..	..	..	< 0.34	..	0.45	0.03	PL
J220402.4-212653	PKS 2201-217	331.010277	-21.448263	Galaxy	327.98	278.75	62.47	..	0.0732	..	Ow95	< 0.41	..	< 0.04	< 0.03	PL

(1) RACS/IPS source name; (2) NED name; (3) IPS Right Ascension (deg); (4) IPS Declination (deg); (5) Legacy Survey DR10 Object type; (6) RACS total flux density (mJy); (7) RACS peak flux density (mJy/beam); (8) IPS Continuum signal to noise; (9) Photometric redshift;(10) Spectroscopic redshift; (11) Spectroscopic redshift uncertainty; (12) Reference catalogue for the spectroscopic redshift; (13) ASKAP NSI; (14) Uncertainty in ASKAP NSI; (15) MWA NSI; (16) Uncertainty in MWA NSI; (17) SED fit (from current work, see Section 3).

Notes. Redshift references (z_ref): Ba99=Baker et al. (1999); Bu70=Burbidge (1970); Dr79=Drinkwater et al. (1997); Du89=Dunlop et al. (1989); Ho08=Holt et al. (2008); Mc96=McCarthy et al. (1996); Ow95=Owen et al. (1995); Pe79=Peterson et al. (1979); Quaia=Gaia-unWISE Quasar Catalog Storey-Fisher et al. (2024); Ti11=Titov et al. (2011).

PL = Power law, PS = Peaked-spectrum, F = Flat, I = Inverted.

https://doi.org/10.1017/pasa.2026.10238 Published online by Cambridge University Press

Table 10. Additional sample

Source	NED name	RAdeg	DEdeg	Object Type	F_tot	F_pk	S/N	z_phot	z_spec	err	z_ref	NSI	err	NSI	err	SED
		J2000		(LS 10)	(mJy)	(mJy)	Cont	PICZL		z_spec		ASKAP	NSI	MWA	NSI	
J213236.6-222229	NVSS J213236-222229	323.152860	-22.374862	..	83.97	69.21	27.93	..	..	..	..	0.43	0.15	0.38	0.04	PL
J213254.3-210942	NVSS J213254-210942	323.226367	-21.161672	..	59.69	57.63	8.90	..	..	..	..	0.64	0.29	0.37	0.06	PL
J213313.9-215402	NVSS J213313-215402	323.308118	-21.900614	..	42.16	41.17	12.97	..	..	..	..	0.53	0.24	0.95	0.15	PL
J213319.8-224421	NVSS J213319-224422	323.332683	-22.739322	Galaxy	124.58	123.04	34.83	0.72	..	..	..	1.29	0.08	1.11	0.13	PS
J213320.2-181051	NVSS J213320-181051	323.334515	-18.181087	Quasar	108.21	105.57	8.50	1.79	..	..	..	0.86	0.24	0.65	0.09	PL
J213409.2-200840	NVSS J213409-200839	323.538430	-20.144485	Galaxy	83.97	29.82	7.17	0.98	..	..	..	0.84	0.32	0.83	0.12	PL
J213418.7-212949	NVSS J213418-212949	323.577937	-21.497180	Galaxy	59.69	36.34	11.77	0.36	..	..	..	0.82	0.23	..	..	PS
J213535.2-204545	NVSS J213535-204546	323.896863	-20.762590	Galaxy	42.16	36.24	10.75	1.18	..	..	..	0.93	0.30	..	..	PS
J213539.8-200016	NVSS J213539-200015	323.916195	-20.004637	..	124.58	37.78	11.42	..	..	..	..	0.63	0.23	..	..	PL
J213551.3-173710	NVSS J213551-173708	323.963947	-17.619564	Galaxy	108.21	63.18	8.29	1.56	..	..	..	0.74	0.29	..	..	PL
J213628.1-230529	NVSS J213628-230530	324.117481	-23.091422	Quasar	37.13	35.47	20.82	1.96	..	..	..	0.97	0.19	..	..	PL
J213656.0-163730	MRC 2134-168	324.233704	-16.625202	..	378.14	367.62	10.64	..	..	..	..	0.81	0.23	0.95	0.06	PS
J213700.3-224847	NVSS J213700-224848	324.251592	-22.813091	Quasar	80.67	80.32	46.76	0.04	..	..	..	0.93	0.09	..	..	PS
J213741.6-174516	NVSS J213741-174515	324.423437	-17.754516	Galaxy	109.54	106.20	14.31	1.42	..	..	..	0.70	0.19	0.86	0.05	PS
J213827.5-230634	NVSS J213827-230635	324.614718	-23.109656	Galaxy	72.85	71.12	18.81	5.82	..	..	..	1.17	0.24	< 0.21	< 0.15	PL
J213830.6-205022	NVSS J213830-205022	324.627880	-20.839507	..	126.58	120.64	17.25	..	..	..	..	0.67	0.31	0.78	0.06	PL
J213914.6-221310	NVSS J213914-221310	324.811219	-22.219504	Quasar	65.34	63.80	37.11	0.64	1.05	0.19	Quaia	0.73	0.14	..	..	PL
J213924.7-200359	NVSS J213924-200358	324.852949	-20.066533	Galaxy	37.03	34.39	7.80	0.14	..	..	..	1.16	0.40	..	..	PL
J213944.6-191225	NVSS J213944-191224	324.936151	-19.207174	Quasar	73.09	70.04	19.02	1.62	..	..	..	0.76	0.15	0.77	0.09	PL
J213958.2-195443	NVSS J213958-195442	324.992716	-19.912086	..	37.62	36.96	8.98	..	..	..	..	1.06	0.32	0.87	0.17	PL
J214027.3-180904	NVSS J214027-180904	325.113779	-18.151279	..	56.59	40.73	6.98	..	..	..	..	0.95	0.40	< 0.00	< 0.13	PL
J214032.6-213956	NVSS J214032-213956	325.135991	-21.665589	Galaxy	127.98	125.57	74.28	3.67	..	..	..	1.05	0.06	0.94	0.06	PS
J214046.8-192357	NVSS J214046-192356	325.195243	-19.399238	Quasar	92.02	90.04	26.45	1.33	1.01	0.07	Quaia	0.94	0.11	..	..	I
J214118.6-185859	NVSS J214118-185858	325.327624	-18.983245	Galaxy	31.54	30.03	9.57	1.46	..	..	..	0.88	0.31	..	..	PS
J214132.1-230213	NVSS J214132-230212	325.384129	-23.037204	Quasar	137.83	117.73	72.06	1.50	..	..	..	0.25	0.22	0.25	0.02	PL
J214154.5-201837	NVSS J214154-201836	325.477475	-20.310343	..	51.36	52.78	23.37	..	..	..	..	1.08	0.15	0.93	0.09	PL
J214158.4-194454	NVSS J214158-194454	325.493341	-19.748524	Quasar	46.23	39.16	17.90	1.88	..	..	..	1.04	0.19	..	..	PL
J214215.8-255126	NVSS J214215-255127	325.566127	-25.857245	Quasar	88.50	86.23	10.01	0.64	..	..	..	3.80	0.49	..	..	F
J214250.0-195153	NVSS J214249-195151	325.708564	-19.864793	Quasar	48.33	46.54	22.65	1.30	..	..	..	0.79	0.18	0.81	0.06	PL
J214320.9-175339	NVSS J214320-175339	325.837470	-17.894259	Quasar	79.52	76.76	15.65	1.56	1.44	0.09	Quaia	1.05	0.20	..	..	F

https://doi.org/10.1017/pasa.2026.10238 Published online by Cambridge University Press

Source	NED name	RAdeg	DEdeg	Object Type	F_tot	F_pk	S/N	z_phot	z_spec	err	z_ref	NSI	err	NSI	err	SED
		J2000		(LS 10)	(mJy)	(mJy)	Cont	PICZL		z_spec		ASKAP	NSI	MWA	NSI	
J214341.4-173705	NVSS J214341-173704	325.922770	-17.618244	Quasar	72.29	70.38	11.90	1.72	..	..	..	0.80	0.30	0.58	0.05	PL
J214355.8-201756	NVSS J214355-201755	325.982907	-20.298975	Quasar	42.25	40.40	19.63	1.47	..	..	..	1.02	0.19	..	..	PS
J214403.1-221742	NVSS J214403-221744	326.013107	-22.295104	Galaxy	49.30	47.75	29.84	0.62	..	..	..	0.72	0.23	..	..	PL
J214409.6-195600	NVSS J214409-195600	326.040327	-19.933403	..	45.92	32.20	16.67	..	..	..	..	0.71	0.26	< 0.34	< 0.13	PL
J214420.3-172202	NVSS J214420-172201	326.084880	-17.367228	Galaxy	135.16	131.90	26.54	0.30	..	..	..	0.52	0.17	0.51	0.04	PL
J214422.9-205741	NVSS J214423-205740	326.095824	-20.961471	..	54.51	53.91	35.51	..	..	..	..	0.68	0.22	0.82	0.08	PL
J214436.3-183650	NVSS J214436-183650	326.151383	-18.614158	Galaxy	65.54	64.20	23.16	1.66	..	..	..	0.90	0.16	..	..	PS
J214443.9-225345	NVSS J214444-225346	326.183297	-22.895886	Galaxy	147.78	144.78	106.37	1.42	..	..	..	1.05	0.05	0.80	0.06	PS
J214516.0-224029	NVSS J214515-224026	326.317059	-22.674976	..	58.54	40.92	11.52	..	..	..	..	1.87	0.39	< 0.02	< 0.06	PL
J214533.4-234633	NVSS J214533-234634	326.389448	-23.776107	..	35.93	24.67	10.49	..	..	..	..	1.95	0.45	< 0.46	< 0.19	PL
J214539.5-231334	NVSS J214539-231335	326.414938	-23.226289	Galaxy	101.98	100.49	70.44	1.34	..	..	..	0.35	0.20	0.55	0.04	PL
J214557.7-184553	NVSS J214557-184552	326.490533	-18.764743	Galaxy	42.67	41.65	17.98	1.56	..	..	..	0.69	0.26	..	..	PS
J214615.8-203846	NVSS J214615-203843	326.565841	-20.646186	Quasar	66.00	54.04	42.25	0.66	0.69	0.07	Quaia	0.71	0.16	0.70	0.07	PL
J214618.5-241422	NVSS J214618-241422	326.577187	-24.239499	Galaxy	115.72	113.30	60.90	1.20	..	..	..	1.07	0.11	0.78	0.09	PS
J214622.4-203536	NVSS J214622-203536	326.593491	-20.593582	Quasar	51.18	47.65	32.57	1.40	..	..	..	1.26	0.14	..	..	PS
J214632.3-232633	NVSS J214632-232633	326.634757	-23.442640	Galaxy	82.78	81.15	48.90	1.49	..	..	..	1.04	0.13	..	..	PL
J214657.2-191339	NVSS J214657-191339	326.738520	-19.227702	Quasar	146.13	138.46	52.13	0.66	..	..	..	0.76	0.08	0.55	0.04	PL
J214716.7-222128	NVSS J214716-222129	326.819745	-22.357856	..	134.58	111.87	70.80	..	..	..	..	0.23	0.23	0.10	0.02	PL
J214728.0-253503	NVSS J214728-253503	326.866827	-25.584234	..	92.03	49.61	7.10	..	..	..	..	5.64	0.70	< 0.00	< 0.10	PL
J214733.7-225527	NVSS J214733-225528	326.890742	-22.924388	..	63.78	62.78	47.24	..	..	..	..	0.89	0.16	0.93	0.09	PS
J214740.1-192730	NVSS J214740-192729	326.917190	-19.458476	Galaxy	63.22	60.99	19.21	0.88	..	..	..	0.84	0.21	0.78	0.10	PL
J214747.8-225315	NVSS J214748-225316	326.949429	-22.887612	Galaxy	42.16	36.08	23.32	0.28	..	..	..	1.33	0.24	..	..	PS
J214811.4-201228	NVSS J214811-201227	327.047864	-20.207980	Galaxy	29.91	28.84	17.52	0.51	..	..	..	1.23	0.29	..	..	PS
J214854.6-190333	NVSS J214854-190332	327.227709	-19.059337	Galaxy	33.55	31.28	9.04	1.45	..	..	..	0.97	0.44	..	..	PS
J215001.7-182226	NVSS J215001-182226	327.507085	-18.374129	Quasar	121.03	118.49	23.07	1.50	1.26	0.28	Quaia	0.77	0.22	0.65	0.17	F
J215018.8-215811	NVSS J215018-215810	327.578340	-21.969865	Galaxy	125.84	121.53	75.04	0.80	..	..	..	0.25	0.25	0.19	0.03	PL
J215036.2-172049	NVSS J215036-172049	327.650846	-17.347121	..	85.64	85.08	14.16	..	..	..	..	0.97	0.34	0.87	0.06	PS
J215050.9-232908	NVSS J215051-232907	327.712401	-23.485575	..	51.33	50.62	29.00	..	..	..	..	0.80	0.31	0.41	0.05	PL
J215103.1-231407	NVSS J215103-231407	327.763299	-23.235386	Galaxy	87.85	86.32	46.51	1.10	..	..	..	0.47	0.25	0.35	0.05	PL
J215156.4-215122	NVSS J215156-215120	327.985017	-21.856229	Quasar	45.98	41.70	30.94	1.84	..	..	..	0.86	0.28	< 0.00	< 0.35	PL

https://doi.org/10.1017/pasa.2026.10238 Published online by Cambridge University Press

Source	NED name	RAdeg	DEdeg	Object Type	F_tot	F_pk	S/N	z_phot	z_spec	err	z_ref	NSI	err	NSI	err	SED
		J2000		(LS 10)	(mJy)	(mJy)	Cont	PICZL		z_spec		ASKAP	NSI	MWA	NSI	
J215207.9-194148	NVSS J215208-194147	328.033155	-19.696698	..	41.09	21.36	6.72	..	..	..	..	1.90	0.62	..	..	PL
J215229.9-230947	NVSS J215230-230948	328.124892	-23.163178	Quasar	37.07	36.21	22.72	1.71	1.64	0.12	Quaia	1.04	0.33	..	..	PS
J215249.5-204422	NVSS J215249-204420	328.206652	-20.739479	Galaxy	39.31	37.99	13.87	5.60	..	..	..	1.09	0.38	1.00	0.18	PL
J215336.3-215031	NVSS J215336-215031	328.401436	-21.842033	..	61.52	60.75	37.65	..	..	..	..	0.83	0.24	< 0.00	< 0.39	PL
J215346.2-223859	NVSS J215346-223900	328.442640	-22.649876	Galaxy	30.87	30.73	6.20	0.38	..	..	..	4.49	0.79	..	..	PL
J215438.6-190220	NVSS J215438-190219	328.660876	-19.038911	Galaxy	87.43	85.91	27.39	1.50	..	..	..	0.77	0.23	0.81	0.05	PL
J215503.3-202612	NVSS J215503-202612	328.764132	-20.436822	..	72.85	70.65	25.64	..	..	..	..	1.19	0.21	0.80	0.10	PL
J215601.7-223907	NVSS J215601-223908	329.007413	-22.652022	Quasar	93.36	92.90	57.45	1.50	..	..	..	1.12	0.17	0.75	0.05	PL
J215850.1-220831	NVSS J215850-220833	329.709061	-22.142214	Galaxy	76.09	75.25	45.24	0.10	..	..	..	0.81	0.34	0.84	0.06	PS

See Table 9 for notes.

Appendix 2. RADIO SEDS

Appendix 2.1 Peaked and Compact Sources

Figure 10 shows the radio SED fitting for every source in the final sample (as shown in Tables 9 and 10) that was classified as compact (an NSI > 0.8 from ASKAP), and had a peaked SED. This list does not include the two already shown in Figures 3 and 4.

Appendix 2.2 Peaked and Slightly Resolved Sources

Figure 11 shows the radio SED fitting for every source in the final sample that was classed as slightly resolved (0.4 < NSI < 0.8 from ASKAP), and had a peaked SED. These were included as sometimes there can be confusion in the beam if there are nearby bright sources.

These sources have an ASKAP NSI between 0.59 and 0.76, so while they are below the cutoff of 0.8, they are still relatively compact.

https://doi.org/10.1017/pasa.2026.10238 Published online by Cambridge University Press

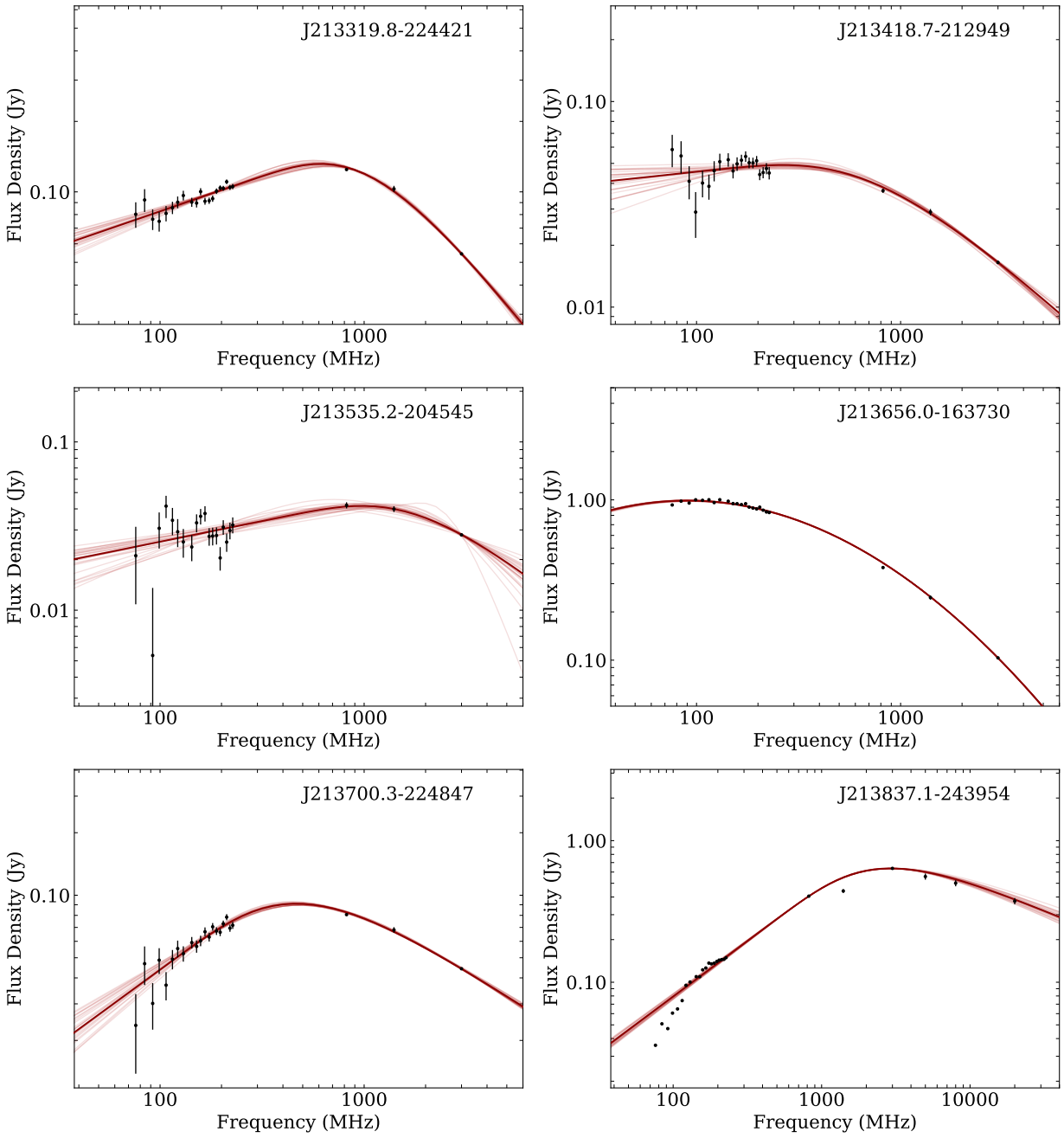
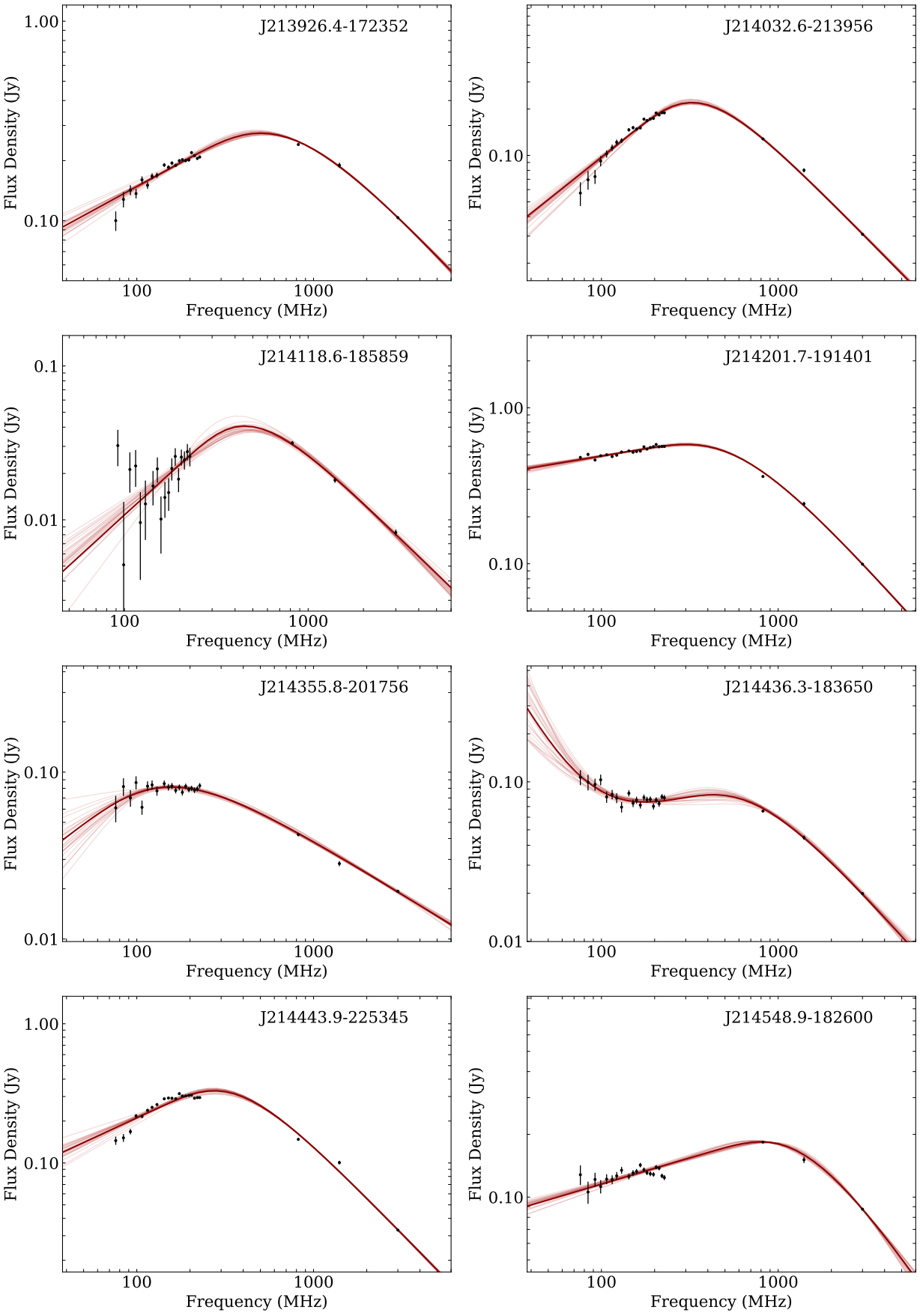
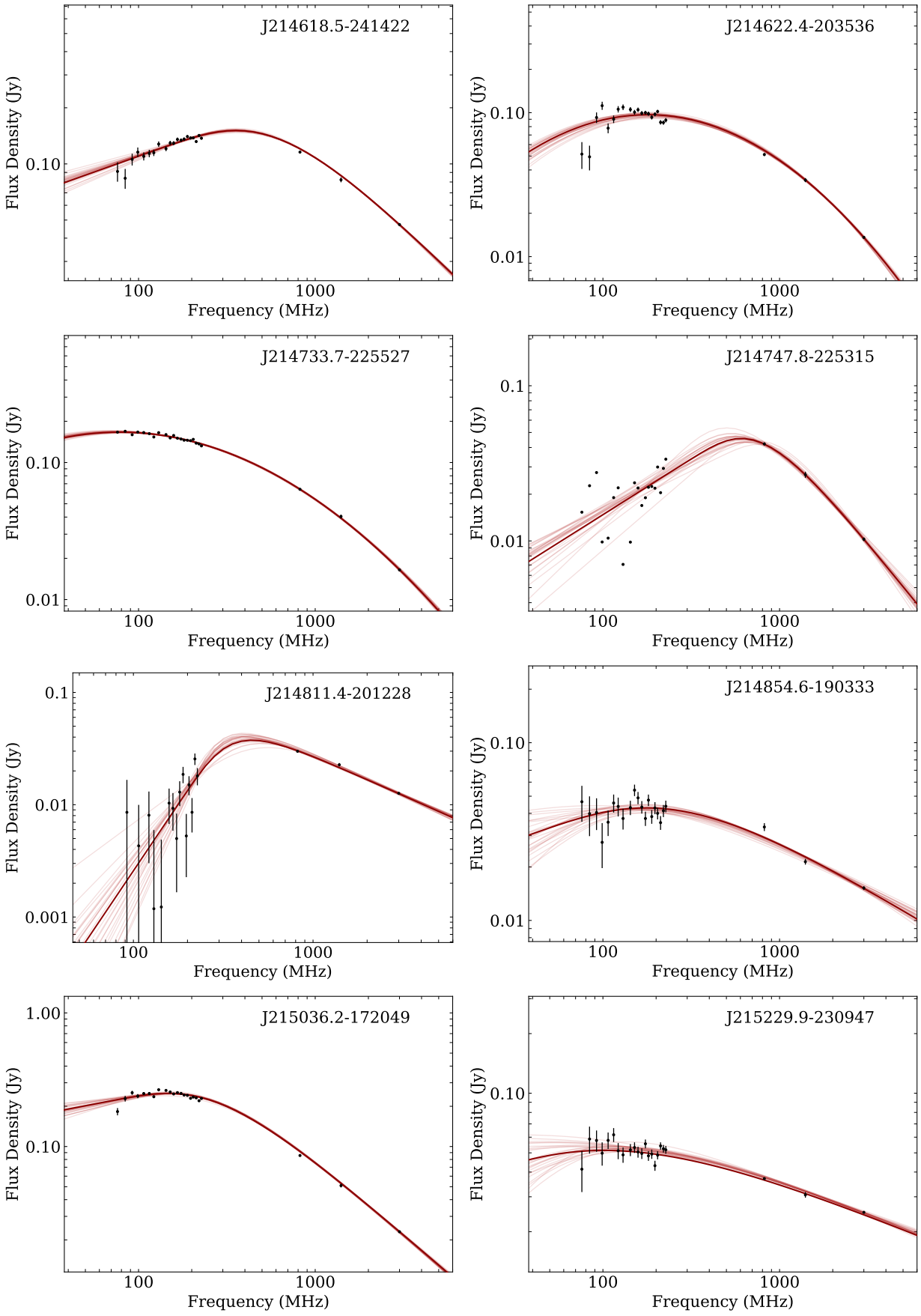


Figure 10. Radio SED fits for all of the compact sources in the final sample that had PS SEDs, not including those already shown in Figures 3 and 4. This figure continues onto the next 3 pages.

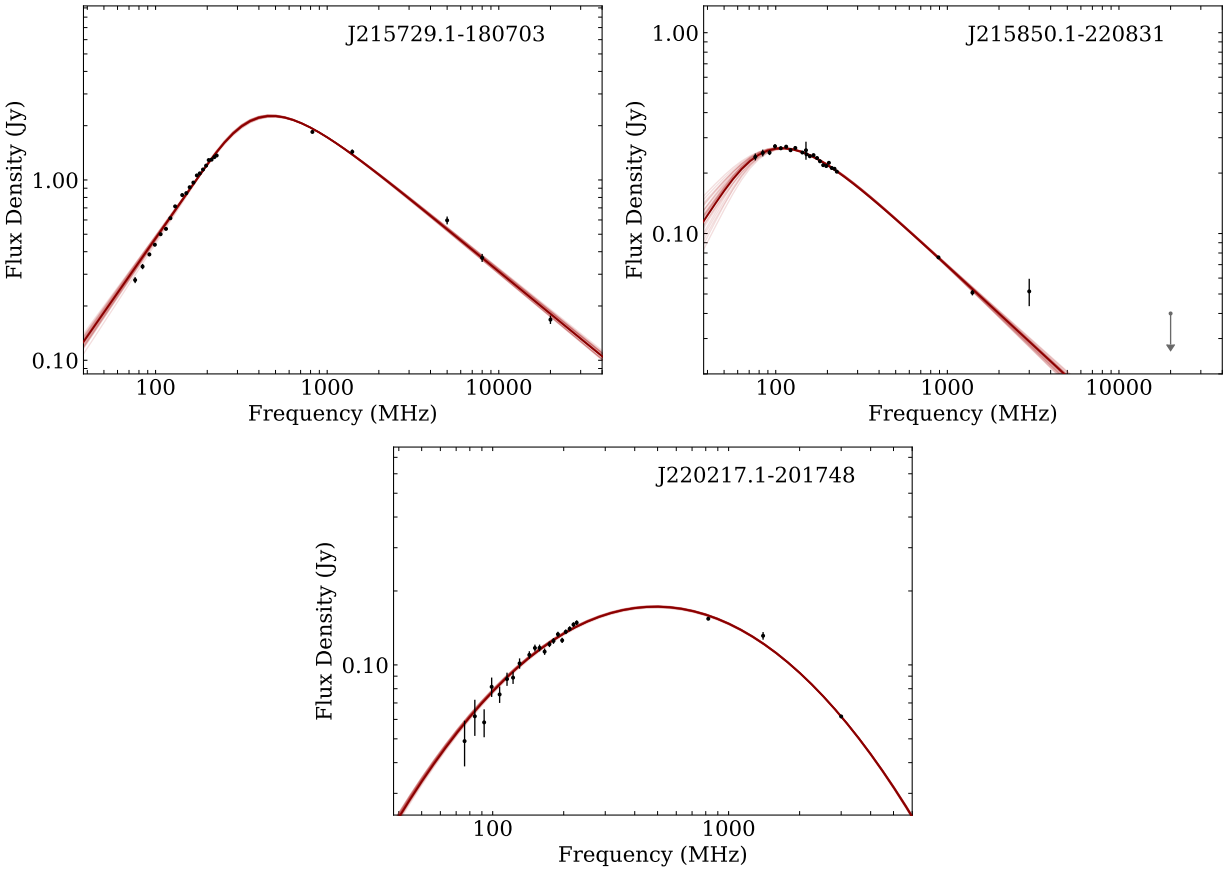
https://doi.org/10.1017/pasa.2026.10238 Published online by Cambridge University Press



https://doi.org/10.1017/pasa.2026.10238 Published online by Cambridge University Press



https://doi.org/10.1017/pasa.2026.10238 Published online by Cambridge University Press



https://doi.org/10.1017/pasa.2026.10238 Published online by Cambridge University Press

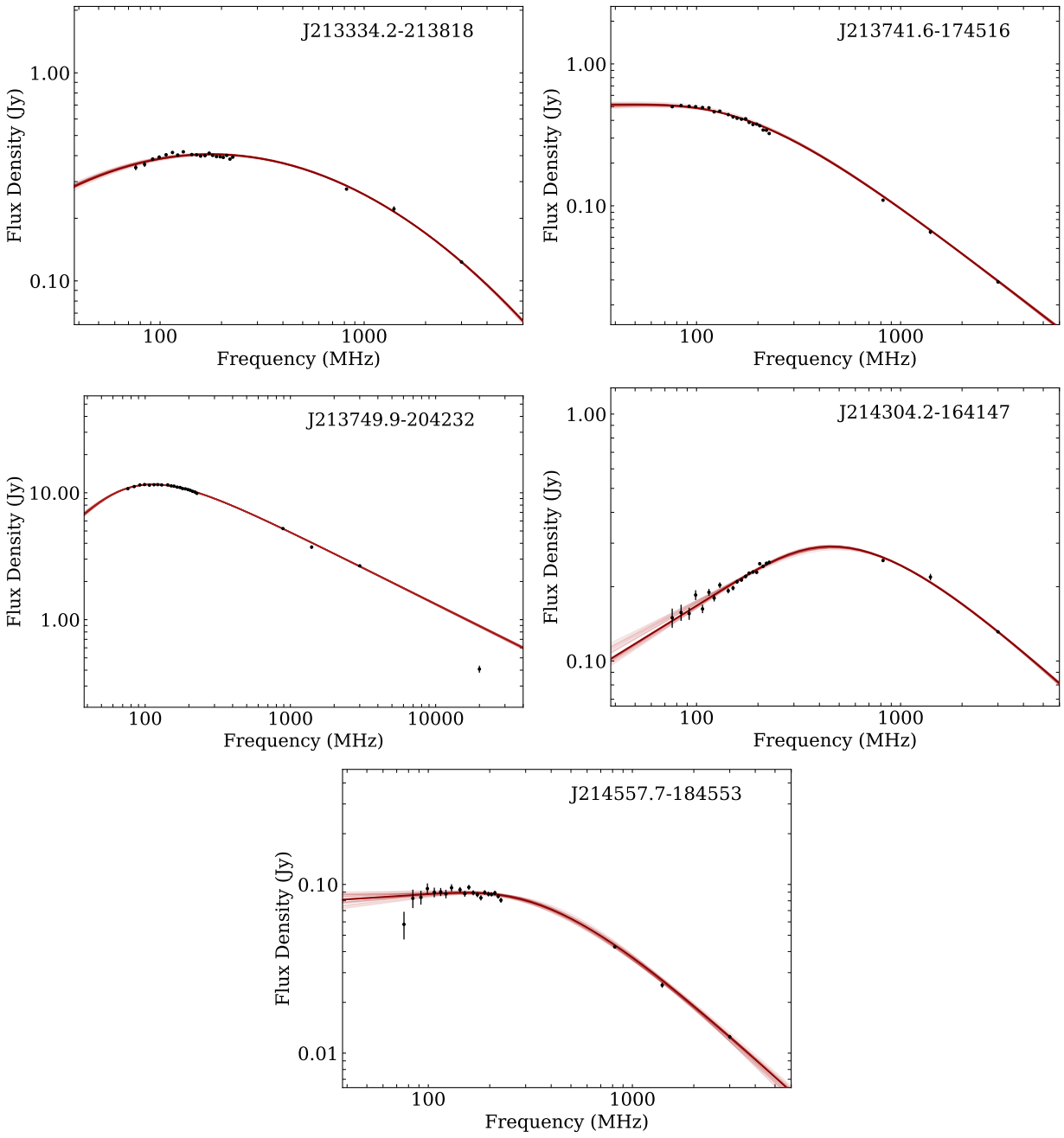


Figure 11. Radio SED fits for all of the slightly resolved sources in the final sample that had PS SEDs.

https://doi.org/10.1017/pasa.2026.10238 Published online by Cambridge University Press